Climate Change and the Mathematics of Transport in Sea Ice

Kenneth M. Golden

Department of Mathematics
University of Utah

Abstract

Polar sea ice is a critical component of our climate system, and an acute indicator of global warming. Understanding fluid and thermal transport in sea ice is fundamental to modeling earth's climate and the polar ecosystems. Electromagnetic transport in sea ice is central to remote sensing of the polar regions, and in assessing the impact of climate change. Here we discuss recent developments in using mathematics to address such issues, and related measurements of transport in sea ice we made on an Antarctic expedition in 2007.

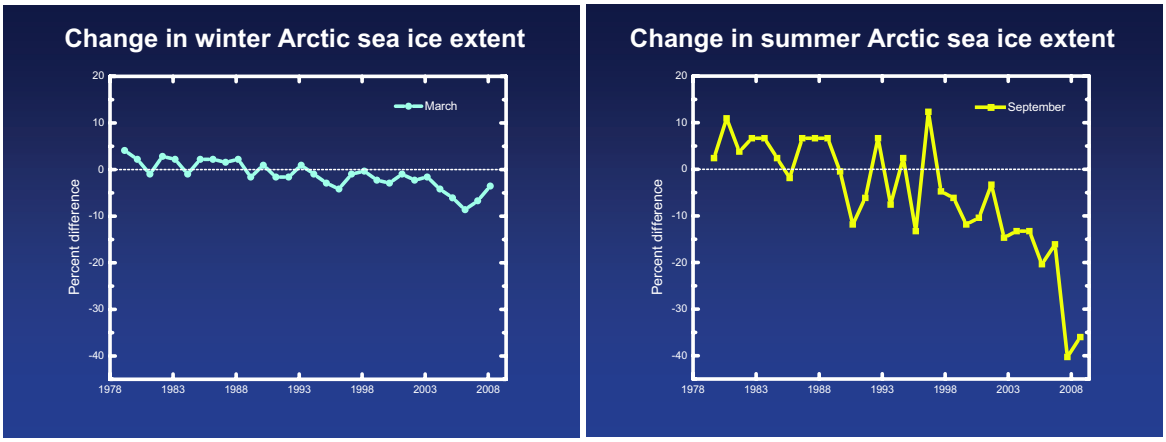

Figure 1: While winter Arctic sea ice extent has decreased modestly over the past thirty years, summer pack ice has experienced a dramatic decline, particularly in last couple years. Some climate scientists wonder if this critical behavior of the system means we have passed through a so-called *tipping point* into a new regime. (Figure courtesy of Donald Perovich.)

Sea Ice and its Role in the Global Climate System

Up until about ten years ago, each summer most of the Arctic Ocean was covered with sea ice of areal extent roughly the same as the continental United States. By 2005, this thick, perennial ice pack had lost the areal equivalent of the US east of the Mississippi River. By the end of the 2007 summer melt season, an area comparable to most of the Midwestern US had been lost as well, and the Arctic ice pack had shrunk by nearly 40 percent from its 1979-2000 average extent. The fabled Northwest Passage was finally open to seafarers for the first time in human memory. These stunning losses in the extent of summer Arctic sea ice represent perhaps the most dramatic, large-scale indicator of global warming on the surface of the earth − so far.

The sea ice pack surrounding the continent of Antarctica is mostly seasonal, meaning it melts in the summer before returning in the cold, dark winter. Will the Arctic become mostly ice-free in summer like the Antarctic? If so, how long will it take? The answers to such questions are critical for global climate. The summer Arctic sea ice pack serves as a major part of earth's polar refrigerator, cooling it and protecting the Arctic Ocean from absorbing too much solar

Figure 2: Newly forming sea ice in Antarctica.

heat. One of the central questions of climate science today is to understand why the Arctic ice pack has declined so precipitously, and to predict how this complex system will evolve in the coming years. In order to see how mathematics can play a role in addressing such fundamental issues, let's first discuss how sea ice forms, explore its material structure, and outline its role in global climate and polar ecosystems.

Sea ice is frozen ocean water, which freezes at a temperature of about $-1.8°$C, or $28.8°$F. Initially, tiny plate-like crystals called *frazil* form near the sea surface. Often they aggregate into slick patches called *grease ice*. When sea ice forms in calm conditions, thin sheets of translucent ice called *nilas* are seen first, which eventually thicken through congelation into gray then white ice in large, undeformed floes. Currents or light winds often push the nilas around so that they slide over each other, a process known as *rafting*. Rafting nilas is shown in Figure 2 on the left. In turbulent conditions typical of the open ocean, the "greasy" frazil suspension undergoes cyclic compression in the wave field, and during compression the crystals can freeze together to form small cakes of slush. They grow larger by accretion and more solid through continued freezing between the crystals, and form plates with raised rims known as *pancake ice* [99]. Patches of grease ice with very small, newly forming pancakes are shown on the right in Figure 2. Larger pancakes are shown in the bottom row of Figure 7. The pancakes in the lower right of Figure 7

are "glued" together in the process of forming larger floes. Sea ice that melts after one season is called *seasonal ice*, and sea ice that survives a summer season is called *multiyear ice*.

During the austral winter the continent of Antarctica, sitting atop the South Pole, is ringed mostly by seasonal ice on the Southern Ocean, with maximal ice extent in September. The Arctic is almost the geographical opposite, with an ocean at the North Pole, surrounded by continents, and covered with both seasonal and multiyear sea ice, of maximal extent in March. Sea ice should be contrasted with icebergs, glaciers, ice sheets, and ice shelves, which all originate on land. The great ice sheets covering Antarctica and Greenland are up to two miles thick, and are composed of glacial ice formed from snow which has been compressed over thousands or millions of years into ice which flows under great pressure.

As a material, sea ice is quite different from glacial ice. When salt water freezes, the result is a polycrystalline composite of pure ice with inclusions of liquid brine, air pockets, and solid salts. As the temperature of sea ice increases, the porosity or relative volume fraction ϕ of brine increases. Brine inclusions on the submillimeter scale are shown in the upper left panel of Figure 7, and its centimeter scale polycrystalline structure is shown in the upper right panel.

Sea ice exhibits a very interesting and important critical phenomenon. For brine volume fractions ϕ below about 5%, sea ice is effectively impermeable to fluid flow, while for ϕ above 5%, it is permeable to fluid flow [19]. This critical brine volume fraction $\phi_c \approx 5\%$ corresponds to a critical temperature $T_c \approx -5^\circ$ for a typical bulk sea ice salinity of 5 parts per thousand, termed the *rule of fives* [38]. When fluid flows through sea ice, transport is facilitated by *brine channels* – connected brine structures ranging in scale from a few centimeters for horizontal slices, to a meter or more in the vertical direction, as shown in the middle panel of Figure 7.

As the boundary layer between the ocean and atmosphere in the polar regions, sea ice is a key player in global climate and the world's ocean system, and is a leading indicator of climate change [100, 53, 94, 86]. The sea ice pack mediates the exhchange of heat, moisture and

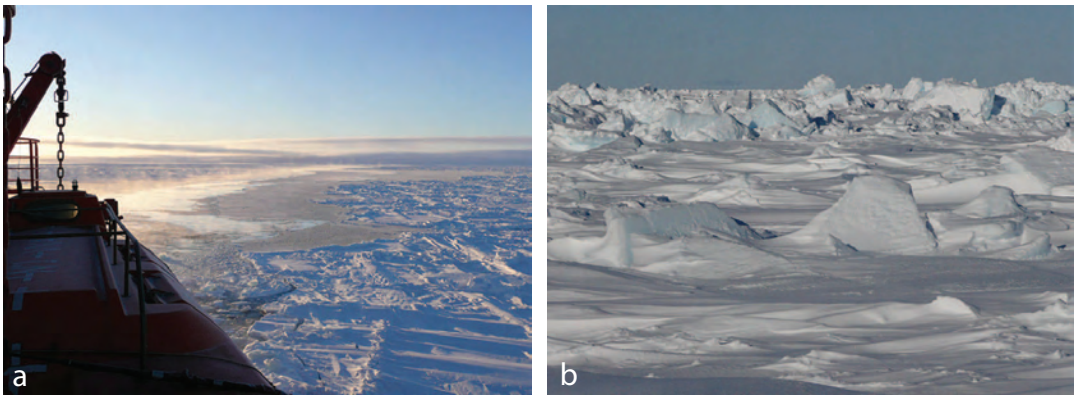

Figure 3: The sea ice pack forms the boundary between the ocean and atmosphere in the polar regions. In (a) sea smoke forms in the track of the icebreaker *Aurora Australis* as heat flows from the warmer ocean to the colder atmosphere. In (b), rough sea ice has a larger drag coefficient than smooth ice, and transfers more momentum from the winds to the ocean below.

momentum between the ocean and atmosphere, the two prinicpal geophysical fluids on earth. For example, as winds push sea ice around on the ocean surface, momentum is transferred to the water below; the rougher the ice, the more efficient the transfer. This process can cause large-scale overturning in the upper ocean, bringing warmer water to the surface. As another example, when sea ice freezes, it rejects cold, dense brine, forming descending plumes in the polar oceans. In the Southern Ocean, this process leads to the formation of Antarctic *bottom water*, which then flows like a complex river through the world's oceans. Another important process in atmosphere−ocean interactions is the transfer of heat between them. In winter when the ocean is warmer, heat flows to the atmsophere through the sea ice itself, which forms an insulating blanket over the ocean, as well as through *leads* or openings in the pack. The thermal conductivity of sea ice is thus an important transport coefficient helping to quantify atmosphere−ocean interactions in coupled climate models.

Roughly speaking, most of the solar radiation which is incident on snow-covered sea ice is reflected, while most of the solar radiation which is incident on darker sea water is absorbed. Sea ice is both ocean sunscreen and blanket, preventing solar rays from warming the waters beneath

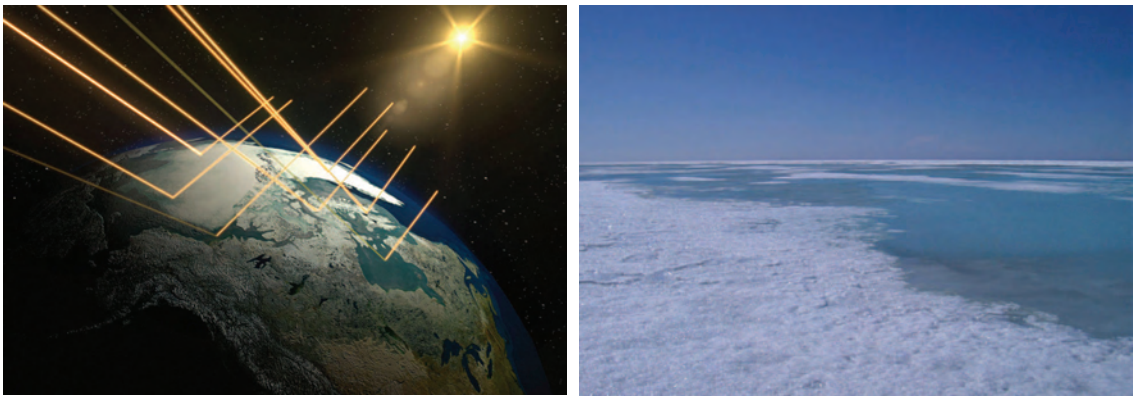

Figure 4: White, ice−covered polar regions are important for reflecting much of the incoming solar radiation during summer, whereas sea water absorbs most of the incident radiation. The relectance, or albedo of the sea ice pack is largely determined by melt ponds on the surface, like those shown on the right in the Arctic in June 2007. Melt pond evolution itself is largely determined by the fluid permeability of the sea ice below, as well as the sun's rays.

and thwarting ocean heat from escaping to warm the air above. The ratio of reflected sunlight to incident sunlight is called *albedo*. While the albedo of snow-covered ice is close to 1 (larger than 0.8), the albedo of sea water is close to zero (less than 0.1). If warming temperatures melt sea ice over time, fewer bright surfaces are available to reflect sunlight, more heat escapes from the ocean to warm the atmosphere, and the ice melts further. As more ice is melted, the albedo of the polar oceans decreases, leading to more solar aborption and warming, which in turn leads to more melting, in a positive feedback loop. It is believed that this so-called *ice-albedo feedback* has played an important role in the marked decrease in Arctic sea ice extent in summer [72]. Thus, even a small increase in temperature can lead to greater warming over time, making the polar regions the most sensitive areas to climate change on earth. Global warming is *amplified* in the polar regions, as shown in Figure 5.

In the summer of 2007, the extent of the summer Arctic ice pack reached a record minimum. Ice mass balance observations show that there was an extraordinarily large amount of melting on the bottom of the ice in the Beaufort Sea during that summer [72]. Calculations indicate that solar heating of the upper ocean was the primary source for the observed melting. An

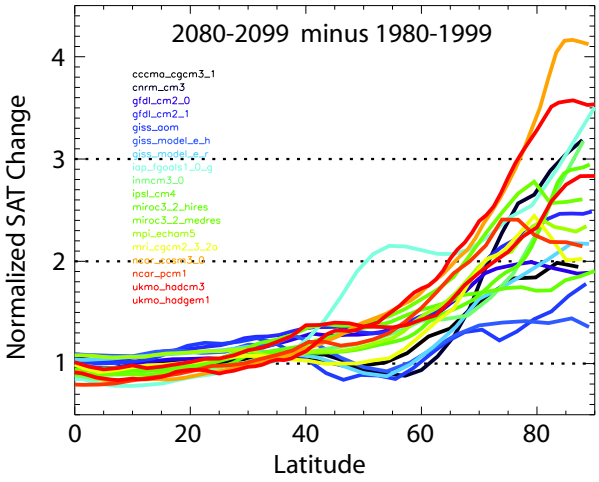

Figure 5: The zonally averaged change in surface air temperature (SAT) normalized by the global average surface air temperature change from a number of climate models for 2080-2099 minus 1980-1999. The normalized air temperature change provides a measure of amplification. For example, a value of 3 indicates 3 times the global average surface air temperature change at that latitude. Climate models consistently show amplified warming in the high latitude Arctic, although the magnitude varies considerably across different models (courtesy of Marika Holland).

increase in the open water fraction resulted in a 500% positive anomaly in solar heat input to the upper ocean, triggering an ice−albedo feedback, accelerating the pack ice retreat. Also of concern is that there has apparently been a significant reduction in the relative amount of thicker, multiyear ice in the Arctic basin. Many authors have recently acknowledged that a relatively younger, thinner ice cover is more susceptible to the effects of atmospheric and oceanic forcing [62, 91, 86]. In the face of predictions for continued warming, the persistence of recent atmospheric and oceanic circulation patterns, and the amplification of these effects through the ice−albedo feedback mechanism, it is becoming increasingly likely that the Arctic Ocean will change from perennially ice-covered to ice-free in the summer [82].

As evidenced from the previous discussion, a key determining factor in predicting the future trajectory of Arctic sea ice is understanding how ice pack albedo evolves. Melt ponds which form on the surface of the ice, as shown on the right in Figure 4, determine its albedo. Whether or not these ponds spread, deepen, or drain, is controlled largely by the fluid permeability of

Figure 6: The rich Antarctic marine ecosystem in supported by photosynthetic algae (d), which give sea ice a brownish or yellowish color (e). Nutrient replenishment for these microbes is controlled by fluid flow through the porous brine microstructure. Krill (c) feed on algae, Emperor penguins (a) feed on krill, and killer whales (b) spy-hop looking for penguins to eat.

the sea ice [22], which is one of the main motivations for our studies of fluid transport in sea ice discussed below.

Another motivation for studying fluid flow in sea ice is the importance of sea ice production from freezing of flooded ice surfaces [61, 1], particularly in the Antarctic, where it is ubiquitous throughout the pack. As snow loading increases during a storm, a pressure head develops. Sea water is forced upward through the sea ice, as constrained by its permeability. Net flux to the surface can occur only if the temperature throughout the entire sea ice layer has exceeded the critical temperature T_c for fluid flow. Once the surface of the ice is flooded, the slushy mix of sea water and snow freezes, which a dominant form of ice production in the Antarctic. In fact, witnessing this process during a powerful winter storm in the Eastern Weddell Sea while on the

Antarctic Zone Flux Experiment (ANZFLUX) in 1994 [65], and watching sea water flood the ice surface in a rather dramatic fashion, was what motivated the author to begin studying fluid transport in sea ice. Recent models have even suggested that with increased polar precipitation accompanying global warming, the Arctic winter sea ice pack could thicken, and that snow-ice production could become more important in the Arctic [74]. Fluid flow through sea ice also facilitates convection-enhanced thermal transport [60, 97], and the input of brine and fresh water into the upper ocean from freezing, melting, and drainage processes [100, 94].

The brine inclusions in sea ice host extensive algal and bacterial communities which are essential for supporting life in the polar oceans, such as krill, which themselves support fishes, penguins, seals, and Minke whales, and on up the food chain to killer whales, leopard seals, and polar bears. Nutrient replenishment processes for sea ice microbes are facilitated by fluid flow through the porous microstrucure. For example, an algal bloom during the Antarctic fall in the Weddell Sea was fueled by nutrient-laden sea water replacing cold dense brine draining from freezing slush at the surface, in a convective overturning process [26]. The bloom effectively shut down, however, once the critical isotherm − above which the ice was impermeable and below which the ice was permeable − passed through the algae layer during the fall freeze-up [38].

One of the fascinating, yet challenging aspects of modeling sea ice and its role in global climate is the sheer range of relevant length scales of structure, over ten orders of magnitude from the submillimeter scale to hundreds of kilometers. In Figures 7 and 8, we show principal examples of sea ice structure illustrating such a range of scales. Modeling sea ice on a large scale depends on understanding the physical properties of sea ice at the scale of individual floes and smaller. Today's climate models challenge even the most powerful super computers to their fullest capacity. However, even the largest computers still limit the horizontal resolution to tens of kilometers and require clever approximations to model the basic physics of sea ice. One of the central themes is how to use information at a smaller scale to predict behavior at a larger scale,

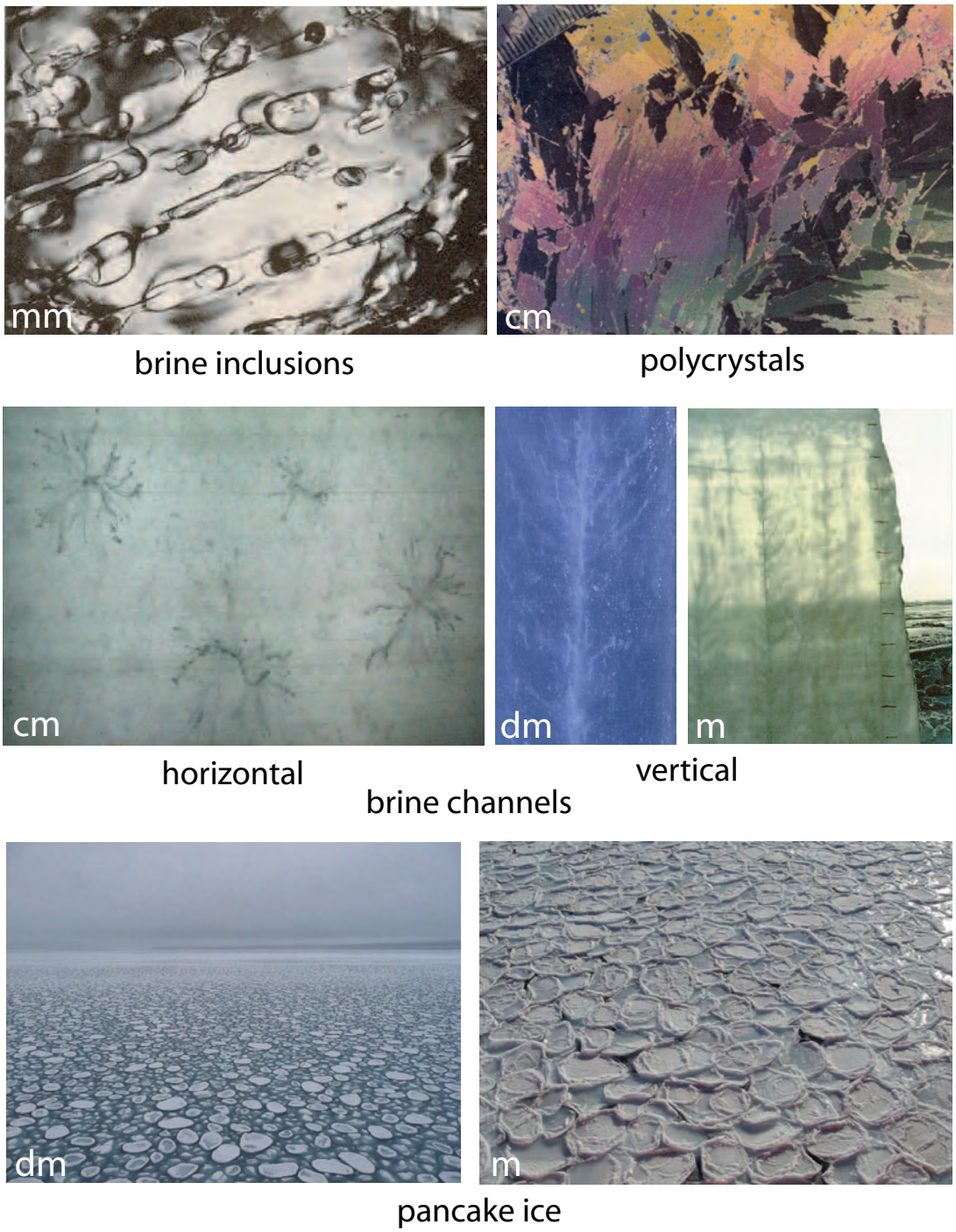

Figure 7: Multiscale nature of sea ice. Sea ice is structured on many length scales, ranging from submillimeter to hundreds of kilometers.

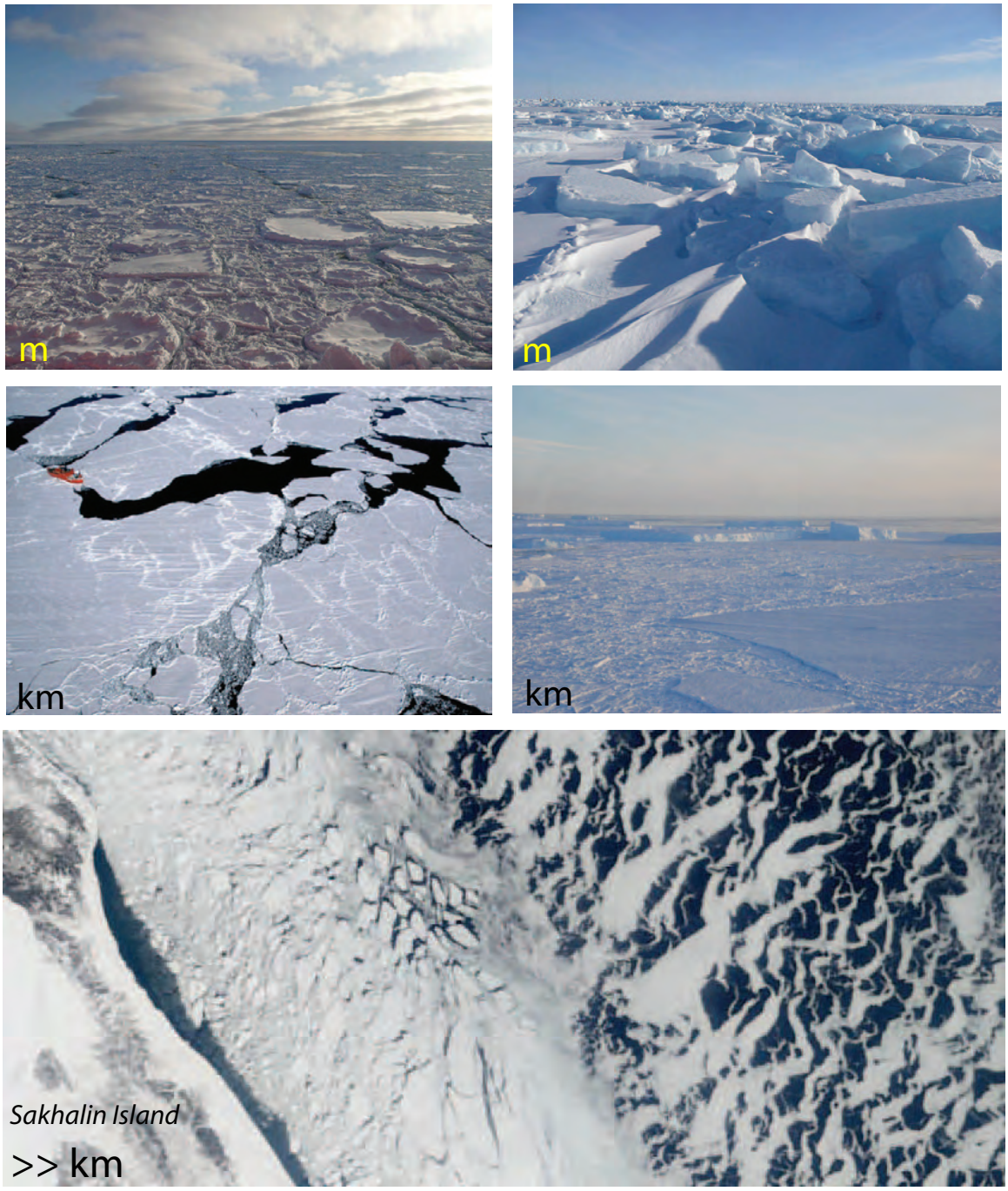

Figure 8: Multiscale nature of sea ice, continued. Pack ice viewed from ice level (top), from a helicopter (middle), and from a satellite (bottom).

such as in classical statistical mechanics. In the sections to follow, we focus on the microphysics of sea ice. That is, we address the fundamental issues of characterizing the brine microstructure and its thermal evolution, and how to use that knowledge to derive information about the bulk transport properties of sea ice relevant to climate models, as well as monitoring climate change. We first consider the fluid transport problem in sea ice, and bounds on the fluid permeability.

Bounds on the Fluid Permeability of Sea Ice

Despite the importance of fluid flow through sea ice in considerations of climate change and polar ecosystems, little attention had been paid to this problem particularly from the theoretical standpoint, with exceptions in [102, 38, 23, 24]. As a first step toward analyzing the dependence of the vertical fluid permeability k on the characteristics of the brine microstructure, such as its volume fraction ϕ, we obtained rigorous upper bounds on $k(\phi)$ [42, 41], which we briefly review.

Consider low Reynolds number flow of a fluid through a porous random medium, occupying a region $\Omega \subset \mathbb{R}^3$. Brine of viscosity μ occupies the brine pore space $\Omega_b \subset \Omega$, having a relative volume fraction ϕ. The solid ice phase occupies the ice grain space $\Omega_i \subset \Omega$, having a relative volume fraction $1 - \phi$. Let $\chi(x)$ be the indicator function of the brine pore space, $\chi(x) = 1$ if $x \in \Omega_b$ and $\chi(x) = 0$ if $x \in \Omega_i$. For an appropriate probability space with translation invariant statistics characterizing the random medium, an *ergodic hypothesis* is satisfied, so that ensemble averaging over realizations is equivalent to an infinite volume limit $|\Omega| \to \infty$ of an integral average over $\Omega \subset \mathbb{R}^3$, denoted by $\langle \cdot \rangle$ [95].

The sea ice temperature T and bulk salinity S determine its brine volume fraction ϕ [100, 21]. Within a given depth range in an ice sheet, the microstructural statistics can be quite uniform over many meters horizontally, so that the conditions above are met. Typically, as with many other porous media [95], there is a microscopic length scale ℓ associated with the medium. For example, the scale over which the two point correlation function obtained from $\chi(x)$ varies, is

a good measure of this length, which is small compared to a typical macroscopic length scale L, such as a sample size or thickness of a statistically homogeneous layer. Then the parameter $\epsilon = \ell/L$ is small, and one is interested in obtaining the effective fluid transport behavior in the limit as $\epsilon \to 0$. To obtain such information, the method of *two-scale homogenization* or *two-scale convergence* [54, 92, 83, 2, 3, 95, 84, 50] has been developed in various forms, based on the identification of two scales: a slow scale x and a fast scale $y = x/\epsilon$. The velocity and pressure fields in the brine, $v^\epsilon(x)$ and $p^\epsilon(x)$ with $x \in \Omega_b$, are assumed to depend on these two scales x and y. The idea is to *average*, or *homogenize* over the fast scale using expansion in powers of ϵ, which leads to a simpler equation describing the overall behavior of the flow.

The velocity and pressure in the brine phase satisfy the Stokes equations,

$$\nabla p^\epsilon = \mu \Delta v^\epsilon, \quad \nabla \cdot v^\epsilon = 0, \qquad x \in \Omega_b(\omega), \tag{1}$$

with the no-slip boundary condition on the pore surface $v^\epsilon(x) = 0$, $x \in \partial\Omega_b$. The first equation in (1) is the steady state fluid momentum equation in the zero Reynolds number limit. The macroscopic equations can be derived through a two-scale expansion, and by averaging the leading order term v_0 of the velocity over y, one obtains

$$v(x) = -\frac{1}{\mu}\, \mathbf{k}\, \nabla p(x), \quad \nabla \cdot v(x) = 0, \tag{2}$$

where $p(x) = p_0(x)$, the leading order term in the expansion of $p^\epsilon(x)$, and $\mathbf{k}$ is the effective permeability tensor. The first equation in (2) is known as Darcy's law and the second is the macroscopic incompressibility condition. These macroscopic equations were obtained in [3, 2] for periodic media through an appropriate limit as $\epsilon \to 0$. We shall be interested in the permeability in the vertical direction $k_{zz} = k$, in units of m^2.

To motivate our results, consider the effective conductivity tensor $\boldsymbol{\sigma}^*$ of a two phase composite with electrical conductivities σ_1 and σ_2 in the volume fractions ϕ and $1-\phi$. The defining equations here are $J = \sigma E$, where J is the current density, E is the electric field, and $\sigma(x)$ is

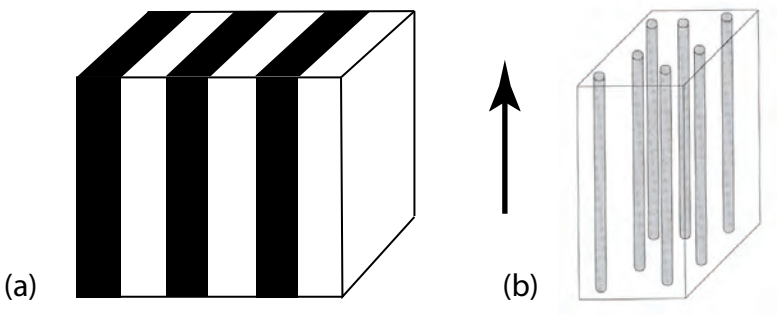

Figure 9: (a) The conductivity of a two phase composite in a vertical electrical field is maximized by laminate structures papallel to the field. (b) The vertical fluid permeability of a porous medium is maximized by vertical pipes with appropriate radii.

the local conductivity taking the values σ_1 and σ_2. The local fields satisfy

$$\nabla \times E = 0, \quad \nabla \cdot J = 0, \tag{3}$$

and the averaged equation $\langle J \rangle = \boldsymbol{\sigma}^* \langle E \rangle$ defines $\boldsymbol{\sigma}^*$, analogous to Darcy's law. Optimal upper and lower bounds on a diagonal component σ^* of $\boldsymbol{\sigma}^*$, such as in the vertical direction, known as the classical arithmetic and harmonic mean bounds (or elementary bounds) were obtained almost one hundred years ago [103],

$$\frac{1}{\frac{\phi}{\sigma_1} + \frac{1-\phi}{\sigma_2}} \;\leq\; \sigma^* \;\leq\; \phi\sigma_1 + (1-\phi)\sigma_2. \tag{4}$$

The bounds are optimal since laminates parallel to the field realize the upper bound, as shown in Figure 9 (a), while laminates perpendicular to the field realize the lower bound.

The following heuristic argument gives insight into much more involved results about fluid permeability. For the fluid problem, we ask what configuration of the pores maximizes k, but a length scale not present for electrical conduction now enters the problem. The electrical conductance g_e of a cylinder of unit length and radius r is $g_e = \pi r^2 \sigma$, where σ is the conductivity of the material. On the other hand, the corresponding fluid conductance g_f of a pipe of unit length and inner radius r is $g_f = \pi r^4/8\mu$. The corresponding *fluid* conductivity $\sigma_f = r^2/8\mu$ thus depends upon the cross sectional area of the pipe. Intuitively, the best arrangement of the

pores to maximize k, which is analogous to $\mu\sigma_f^*$ with σ_f^* the effective fluid conductivity, is in vertical pipes, as shown in Figure 9 (b). Viewing sea ice as a two phase composite with the fluid conductivities $\sigma_2 = 0$ for the ice phase and $\sigma_1 = r^2/8\mu$ for uniformly sized brine inclusions, yields from the upper bound in (4) a *pipe bound*, $k \leq \phi[a(\phi)]^2/8$, with mean brine inclusion horizontal cross-sectional radius $a(\phi) = 7 \times 10^{-5} + (1.6 \times 10^{-4})\phi$ meters [71].

The simple pipe bound, based on uniformly sized pipes whose radii increase with ϕ or T, captures laboratory data on relatively small samples [42]. However, when considering Arctic field data where a broader range of inclusion length scales is relevant, a few large connected brine structures can dominate a measurement and some of the data lie outside the bound. We must consider generalizations which allow for a distribution of radii. The derivation of such bounds [96, 42, 41], which rigorously extend the arithmetic bound in the electrical case to fluid problems and give more information as well, employs diffusion processes in the pore space.

Consider the problem of a tracer diffusing in the fluid phase $\Omega_b \subset \Omega \subset \mathbb{R}^3$ of a porous medium. The tracer reacts with partially or completely absorbing *traps* on the boundary $\partial\Omega_b$ of the pore space. The traps themselves may represent particulate sediment entrained in the sea ice having nutritive organic content for enzymatic foraging by bacteria [42]. Let $c(x,t)$ with $x \in \Omega_b$ be the time dependent concentration of the reactant governed by the diffusion equation and boundary condition

$$\frac{\partial c}{\partial t} = D\Delta c + G, \;\; x \in \Omega_b, \qquad D\frac{\partial c}{\partial n} + \eta c = 0, \;\; x \in \partial\Omega_b, \tag{5}$$

where D is the diffusion coefficient of the reactant in the fluid, η is a positive surface reaction rate constant, G is a generation rate of reactant per unit trap-free volume, and n is the unit outward normal from the pore space. A dimensionless surface rate constant $\eta^* = \eta\ell/D$, where ℓ is a characteristic pore length, can be used to distinguish different regimes of influence: diffusion-controlled for $\eta^* \gg 1$, and reaction-controlled for $\eta^* \ll 1$. In the diffusion-controlled regime, a reactant will typically diffuse in the pore space for much longer than the characteristic time

associated with the surface reaction. In the limit of infinite surface reaction $\eta \to \infty$, the boundary condition becomes a perfectly absorbing *Dirichlet condition*, with $c = 0$ on $\partial\Omega_b$ wherever the traps are located.

In the diffusion-controlled limit, we consider the steady state problem where the rate of removal of the reactant by the absorbing boundaries is exactly compensated by the production rate per unit volume G of the reactant. Then the diffusion equation (5), or mass conservation equation, becomes a Poisson equation $D\Delta c = -G$, $x \in \Omega_b$ with $c = 0$ for $x \in \partial\Omega_b$. The macroscopic behavior is derived again through a two-scale expansion for $c^\epsilon(x) = c(x, y)$ with $y = x/\epsilon$. The leading order function $c_0(x, y)$ satisfies $D\Delta_y c_0(x, y) = -G(x)$, $x \in \Omega_b$ and $c_0(x, y) = 0$ for $x \in \partial\Omega_b$. A scaled concentration u defined by $c_0(x, y) = D^{-1}G(x)u(y)$ solves

$$\Delta_y u(y) = -1, \;\; y \in \Omega_b, \qquad u(y) = 0, \;\; x \in \partial\Omega_b, \tag{6}$$

where $u = 0$ in the region Ω_i. Averaging the defining relation for u yields the macroscopic constitutitve relation for the trapping problem, $G(x) = \gamma DC(x)$, where C is an averaged concentration $C(x) = \langle c_0(x, y)\rangle$ and γ is the *trapping constant*,

$$\gamma^{-1} = \langle u(y)\chi(y)\rangle. \tag{7}$$

The *mean survival time* τ of a Brownian particle in the pore space is $\tau = 1/\gamma\phi D = \langle u\rangle/\phi D$. For the trapping constant, we are interested in a variational lower bound,

$$\gamma \geq \langle \nabla v(x) \cdot \nabla v(x)\, \chi(x)\rangle^{-1}, \quad \forall v \in \{\text{ergodic } v(x) : \Delta v(x) = -1, \; x \in \Omega_b\}. \tag{8}$$

An appropriately constructed trial field yields a general two-point *void lower bound* [96] for trapping, $\gamma \geq \phi_S^2/\ell_P^2$, where ℓ_P is a pore length scale defined in terms of the two point correlation function of the porous medium, and ϕ_S is the trap volume fraction. It is somewhat surprising that effective properties characterizing diffusion in a porous medium, such as γ, are closely related to effective properties characterizing bulk transport from flow. In fact, for any ergodic

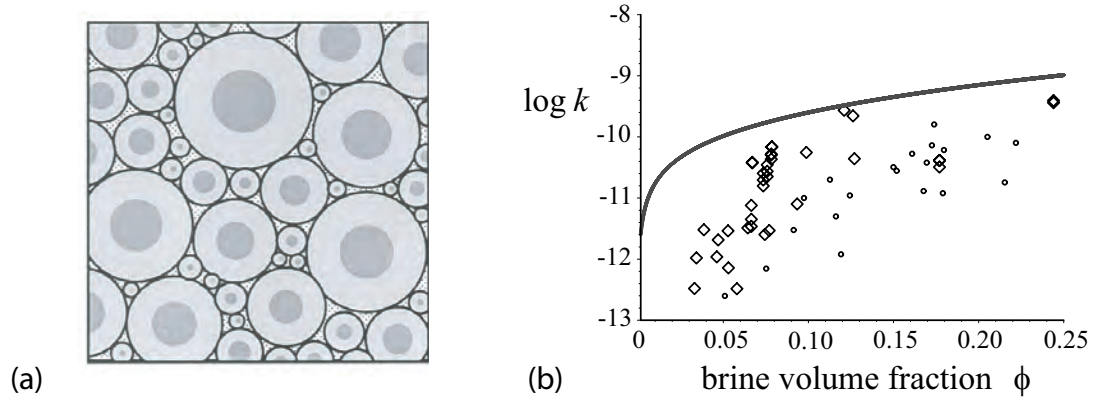

Figure 10: (a) Hashin-Shtrikman coated cylinders provide an optimal geometry which attain the two point void upper bound for the vertical fluid permebaility. (b) The lognormal pipe bounds capture all our lab and field data on the vertical permeability of sea ice.

porous medium, possibly anisotropic, $\mathbf{k} \leq \gamma^{-1}\mathbf{I}$, or equivalently, $(\gamma^{-1}\mathbf{I}-\mathbf{k})$ is a positive definite, symmetric, second order tensor [95].

In the theory of composite materials, the Hashin-Shtrikman bounds [49] are important in providing optimal estimates on effective transport properties using the volume fractions as well as the two point correlation function. The bounds are attained with arrays of coated spheres in $d = 3$ or coated cylinders in $d = 2$, filling all space. The two-point void lower bound above can be evaluated [96] for coated cylinder geometries, i.e., brine-filled vertical ice pipes for the sea ice problem, with appropriate distributions of inclusion radii R_I, as shown in Figure 10 (a). Using the inequality relating the permeability tensor to the trapping constant yields an optimal, rigorous upper bound,

$$k \leq \frac{\phi \langle R_I^4 \rangle}{8 \langle R_I^2 \rangle} \, . \tag{9}$$

Measured brine inclusion cross-sectional areas A have been found to obey a lognormal distribution [71]. Then $z = \ln A$ has a normal probability density with mean α and variance ρ^2,

$$P(z) = \frac{1}{\sqrt{2\pi\rho^2}} \, e^{-(z-\alpha)^2/2\rho^2}. \tag{10}$$

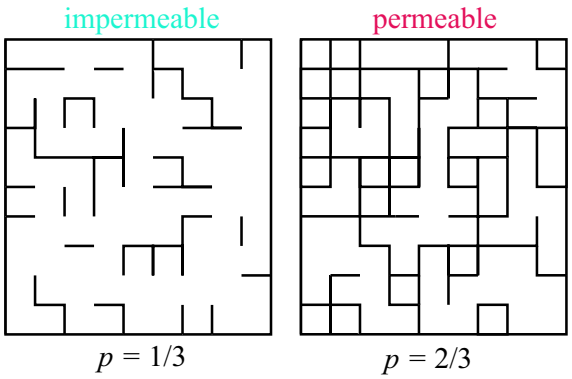

Figure 11: The two dimensional square bond lattice below its percolation threshold at $p_c = 1/2$ in (a), and above its threshold in (b).

We evaluated the moments in (9) using the lognormal distribution, yielding [41]

$$k(\phi) \leq \frac{\phi}{8\pi} \langle A(\phi) \rangle \, e^{\rho^2}. \tag{11}$$

With variance [71] $\rho^2 \approx 1$ and $\langle A(\phi) \rangle = \pi a^2(\phi)$ as above, the *lognormal pipe bound* in (11) captures our Arctic field data, as well as the lab data, as shown in Figure 10 (b). The field data were taken near Barrow, Alaska in a hydrological bail test [24, 22], where a cylindrical hole is drilled, a tube is inserted to seal off horizontal flow, and time series measurements of the water level are used to estimate the permeability of the ice under the hole.

Percolation Theory for Sea Ice

Percolation theory [12, 89, 95, 84, 36] has been used to model disordered materials where the connectedness of one phase dominates effective behavior. Examples range from porous rocks and bubbly glacial ice to semiconductors and carbon nanutube composites. Consider the square ($d = 2$) or cubic ($d = 3$) network of bonds joining nearest neighbor sites on the integer lattice $\mathbb{Z}^d$. We'll initially consider the problem of electrical transport through the network, and then fluid transport. The bonds are assigned electrical conductivities $\sigma_0 > 0$ (open) or 0 (closed) with probabilities p and $1 - p$. Groups of connected open bonds are called open clusters, and

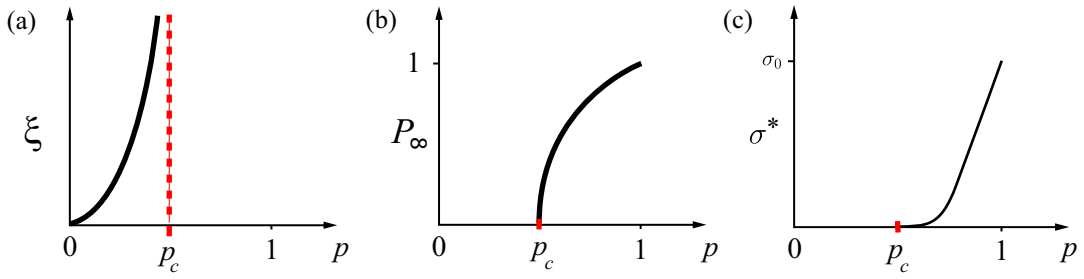

Figure 12: (a) The correlation length diverges as $p \to p_c^-$. (b) The infinite cluster density $P_\infty(p)$ vanishes below p_c, and takes off with power law behavior above p_c. (c) Below p_c, there is no bulk transport, and above p_c the tranpsort coefficient takes off with a different power law.

the average cluster size grows as p increases. The striking feature of this model is that there is a critical probability p_c, $0 < p_c < 1$, called the *percolation threshold*, where an infinite cluster of open bonds first appears. In $d = 2$, $p_c = \frac{1}{2}$, and in $d = 3$, $p_c \approx 0.25$.

The infinite cluster density $P_\infty(p)$ is defined as the probability that the origin (or any point, by translation invariance) is contained in the infinte cluster, whose graph is shown in Figure 12 (a). The two-point function $\tau(x, y)$ measures the probability that two points x and y belong to the same open cluster. As $|x - y| \to \infty$, $\tau(x, y) \sim exp(-|x - y|/\xi)$, where ξ is called the correlation length, which is a measure of the scale of connectedness. The correlation length diverges as p increases toward p_c and the infinite cluster forms, as shown in Figure 12 (b). In the neighborhood of p_c, $P_\infty(p)$ and $\xi(p)$ exhibit power laws, with

$$P_\infty(p) \sim (p - p_c)^\beta, \;\; p \to p_c^+, \qquad \xi(p) \sim (p_c - p)^{-\nu}, \;\; p \to p_c^-, \tag{12}$$

where β and ν are *universal* critical exponents which are believed to depend only on dimension, and not on the details of the lattice. In $d = 3$, $\beta \approx 0.41$ and $\nu \approx 0.88$ [89].

Let $\sigma^*(p)$ be the effective conductivity of this random resistor network in the vertical direction, as defined by Kirchoff's laws in the infinite volume limit [15, 31]. For $p < p_c$, $\sigma^*(p) = 0$, as shown in Figure 12 (c). For $p > p_c$ near the threshold, $\sigma^*(p)$ exhibits power law behavior,

$$\sigma^*(p) \sim \sigma_0 (p - p_c)^t \;, \quad p \to p_c^+, \tag{13}$$

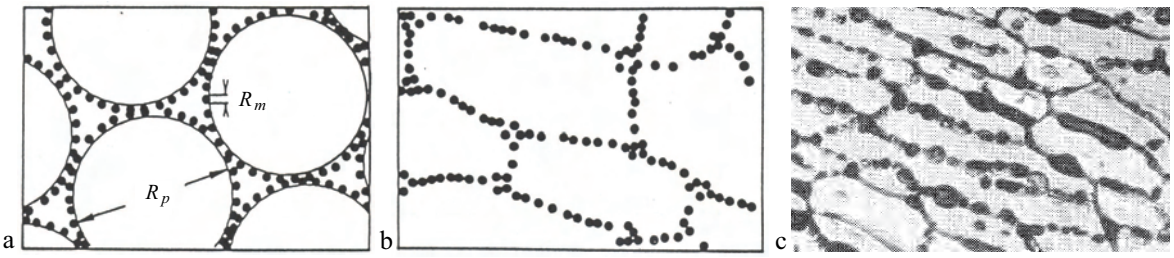

Figure 13: (a) A powder of large polymer spheres mixed with smaller metal spheres [56]. (b) When the powder is compressed, its microstrucure is similar to that of sea ice in (c).

where t is the conductivity critical exponent. For lattices, t is believed to be universal, depending only on d. The corresponding fluid permeability $\kappa^*(p)$ of the lattice, where the bonds are open or closed pipes of fluid conductivity $\kappa_0/\mu = r_0^2/8\mu$, behaves like

$$\kappa^*(p) \sim \kappa_0(p - p_c)^e \,, \quad p \to p_c^+, \tag{14}$$

where e is the fluid permeabilty exponent. For lattices, it is believed that $e = t$ [95, 48, 9]. In $d = 2$ [89, 84], $t \approx 1.3$, and in $d = 3$, it is believed [89, 95] that $t \approx 2.0$. There is also a rigorous bound [30, 31] that $t \leq 2$.

In view of the apparent critical behavior of brine drainage in columnar sea ice depending on whether ϕ is above or below about 0.05 [100], it was reasonable to try and find a percolation theoretic explanation. However, with $p_c \approx 0.25$ for the $d = 3$ cubic bond lattice, it was apparent that key features of the geometry of the brine microstructure in sea ice were being missed by lattices. In [38] $\phi_c \approx 0.05$ was identified with the critical probability in a continuum percolation model for compressed powders [56] which exhibit microstructural characteristics similar to sea ice. The identification explained the rule of fives, as well as data on algal growth and snow-ice production. The compressed powders, shown in Figure 13, were used in the development of so-called *stealthy* or radar absorbing composites.

When we applied the compressed powder model to sea ice about a decade ago, we had no *direct* evidence that the brine microstructure undergoes a transition in connectedness at a crit-

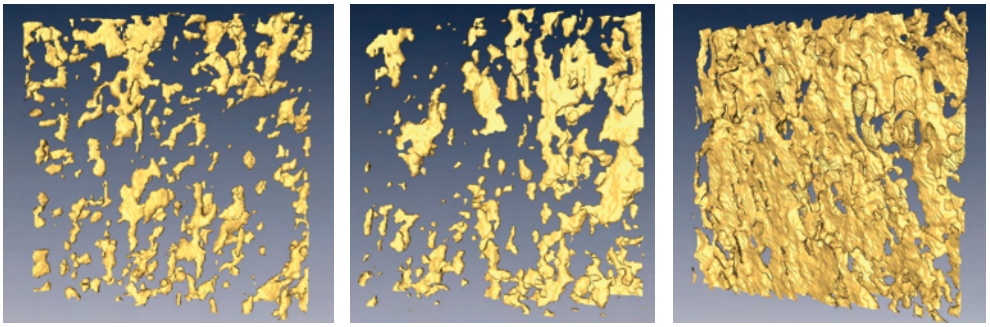

Figure 14: X-ray CT volume rendering of brine layers within a lab-grown sea-ice single crystal with S = 9.3 ppt. The (non-collocated) 8 × 8 × 2 mm sub-volumes illustrate a pronounced change in the micro-scale morphology and connectivity of the brine inclusions during warming.

ical brine volume fraction. This lack of evidence was due partly to the difficulty of imaging and quantitatively characterizing the brine inclusions in three dimensions, particularly the thermal evolution of their connectivity. Through X-ray computed tomography and pore structure analysis [41, 77] we have now analyzed critical behavior of the thermal evolution of brine connectedness in sea ice single crystals, over a temperature range from -18° C to -3° C. We have mapped three dimensional images of the brine phase onto graphs and analyzed their connectivity as functions of temperature and sample size. Realistic network models of brine inclusions can be derived from porous media analysis of 3-D micro-tomography images. Approaches include the well-established 3DMA package (3-Dimensional Medial Axis, e.g [57, 58, 79] and the developmental Tight Dual Model [28, 27]. We have worked closely with developers of both packages [76, 78, 41]. In both cases, a 3-D graph of nodes and edges is derived from the pores and throats. In general terms, the steps are: (1) represent the pore space by a polyhedral complex; (2) decompose this digital pore space into pores and throats, and compute individual characteristic radii; (3) map these to nodes and edges, tagged with their respective radii. The resulting graphs enable imbibition and drainage characterization [28, 27], connectivity and critical path analyses (see below) [41, 78, 76].

An example of how brine morphology and connectivity evolves with temperature is shown in Figure 14. X-ray CT has provided new insight into small-scale, intra-crystalline brine layer connectivity. Our work provides the first direct observation of an onset in connectivity over this scale ($\approx$ 1 cm). Notably, the thermal evolution of pore morphology that we observe is more complex than the classic model [94, 100], a transition from brine sheets to cylindrical to spheroidal inclusions, which underlies a range of porosity models [94, 100].

While percolation theory has been applied to disordered composites for fifty years, key functions such as the percolation probability (which equals 0 for $p < p_c$ and equals 1 for $p > p_c$), the infinite cluster density, the correlation length, and their critical exponents, have been computed only for idealized models, like the square or cubic lattice, and *not* for real materials. In general, it is difficult not only to image the microstructure of complex disordered media, but to conveniently vary the volume fraction of the connected phase in which one is interested, such as the pore space in rocks or the doping in semiconductors. However, for sea ice, by changing the temperature of a single sample we can significantly vary the brine volume fraction. In [77], we have computed these functions from our three dimensional imaging of the pore-space evolution. For example, from analysis of the two point connectivity function, we have generated a graph of the correlation length quite similar to Figure 12 (a).

We have also used our data to find anisotropic percolation thresholds using *finite-size scaling*. Rather than attempting to compute very sensitive parameters such as the percolation threshold or critical exponents from real data and its variation in volume fraction, finite-size scaling is a technique from physics where one exploits the dependence of functions of interest on sample size to obtain such results. In our case, a key relation is

$$P_\infty(p_c, L) \sim L^{-\beta/\nu}, \qquad L \to \infty. \tag{15}$$

In single crystals of sea ice the brine microstrucure is highly anisotropic, with inclusions usually arranged in layers. Using three different approaches, we have employed finite-size scaling to

obtain anisotropic critical porosities of $4.6 \pm 0.7\%$ in the vertical direction, and laterally, $9 \pm 2\%$ parallel to the layers and $14 \pm 4\%$ perpendicular to them. The value of about 4.6% in the vertical direction for single crystals should be smaller than the threshold of about 5% for bulk connectivity, which it is.

Now we consider the application of percolation theory to understanding the fluid permebaility of sea ice. In the continuum, the permeability and conductivity exponents e and t can take non-universal values, and need not be equal, such as for the three dimensional Swiss cheese model [95, 48, 9]. Continuum models have been studied [95, 48, 9] by mapping to a lattice with a probability density $\psi(g)$ of bond conductances g. Non-universal behavior can be obtained when $\psi(g)$ is singular as $g \to 0^+$. However, for a lognormal conductance distribution arising from intersections of lognormally distributed inclusions, as in sea ice, the behavior is *universal*, which has been verified numerically [9]. Thus $e \approx 2$ for sea ice.

The permeability scaling factor k_0 for sea ice, analogous to κ_0 in (14), is estimated using critical path analysis [25, 43]. For media with g in a wide range, the overall behavior is dominated by a critical, *bottleneck* conductance g_c, the smallest conductance such that the critical path $\{g : g \geq g_c\}$ spans the sample. With most brine channel diameters [100] between 1.0 mm and 1.0 cm, spanning fluid paths have a smallest, characteristic radius $r_c \approx 0.5$ mm, and we estimate k_0 by the pipe-flow result ${r_c}^2/8$. Thus

$$k(\phi) \ \sim \ 3\,(\phi - \phi_c)^2 \ \times 10^{-8} \ \mathrm{m}^2, \quad \phi \to \phi_c^+. \tag{16}$$

In Figure 15 (c), field data with ϕ in $[0.055, 0.15]$, just above $\phi_c \approx 0.05$ [38, 73], are compared with (16), showing close agreement. A best fit for e of 1.94 was obtained from other data [69]. The striking result that for sea ice, $e \approx 2$, the universal *lattice* value in three dimensions [95, 30], is due to the general lognormal structure of the brine inclusion distribution function [71]. The general nature of our results suggests that similar types of porous media, such as saline ice on extraterrestrial bodies [93], may also exhibit universal critical behavior.

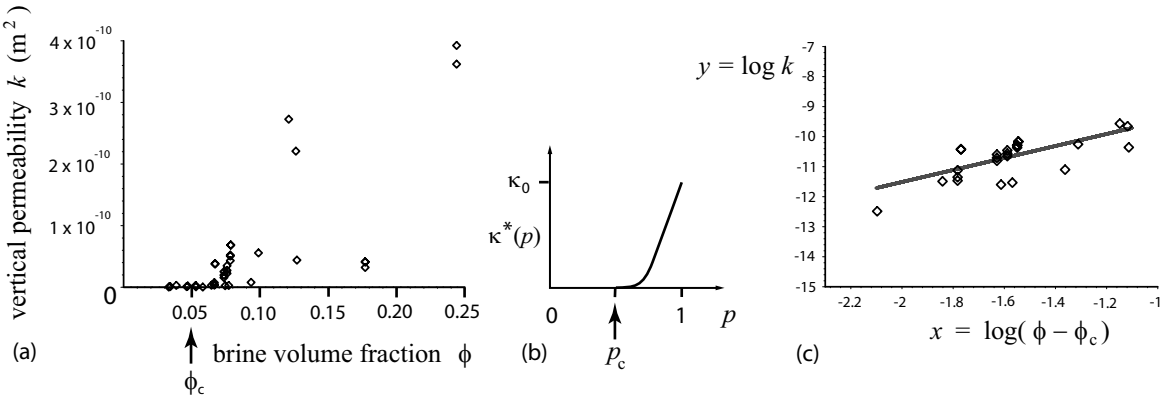

Figure 15: (a) Data for k taken *in situ* on Arctic sea ice, displayed on a linear scale. (b) The effective permeability $\kappa^*(p)$ in a lattice percolation model, displayed on a linear scale. (c) Comparison of Arctic permeability data in the critical regime (25 data points) with percolation theory in (16). In logarithmic variables the predicted line has the equation $y = 2\,x - 7.5$, while a best fit of the data yields $y = 2.07\,x - 7.45$, assuming [38, 73] $\phi_c = 0.05$.

To model $k(\phi)$ over all porosities, not just near the percolation threshold, we consider features of the brine phase present over the full range − some degree of connectivity, particularly on small scales, and self-similarity. The basic unit of sea ice microstructure is an ice grain surrounded by brine and ice, having substructure itself on smaller scales. Hierarchical, self-similar models of spheres or other grains surrounded by smaller spheres, and so on, with brine of conductivity σ_w in the pore spaces, have been used to describe the transport properties of sedimentary rocks [85, 105]. Such microstructures are similar to those shown in Figure 10 (a), except in this case the basic elements are brine coated spheres of ice. Effective medium theory [85, 105] gives Archie's law $\sigma = \sigma_w \phi^m$ as the conductivity of the model with exact results for the exponent m, such as $m = 3/2$ for spherical grains. The corresponding permeability exponent [105] is $2m$, so that with k_0 as above and $m = 3/2$, the simplest hierarchical model yields

$$k(\phi) = 3\ \phi^3\ \times 10^{-8}\ \ \mathrm{m}^2. \tag{17}$$

In Figure 16 (a) the full *in situ* data set is compared to this theoretical prediction, with close agreement. From photomicrographs of marine sand microstructures [52], compacted platey sand

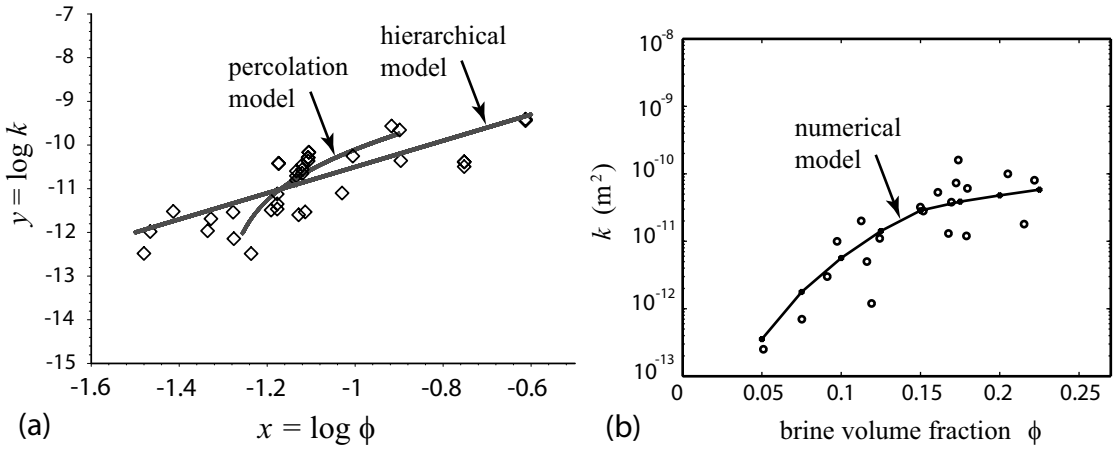

Figure 16: (a) Comparison of Arctic permeability data (37 data points) with our theoretical prediction in (17). In logarithmic variables the predicted line has the equation $y = 3x - 7.5$, while a best fit of the data yields $y = 3.05x - 7.50$. The lab data on artificially grown sea ice [23] give a best fit of $y = 3.1x - 7.7$. (b) Comparison of lab data with numerical simulation.

appears the most similar to the cellular substructure of sea ice. In this case, $2m \approx 3.04$, which is closer to the best fit of 3.05 from our field data. For calcite aggregates and Fontainebleau sandstone, a cubic power law like (17) agrees closely with permeability data for porosities above about 10% [55], with an exponent $2m \approx 3.05$ for Fontainebleau sandstone [11].

Our results show that the parameters characterizing fluid transport in sea ice are almost the same as in some crustal, sedimentary rocks [55]. Both types of media exhibit critical behavior near a percolation threshold, with $\phi_c \approx 5\%$ for sea ice, and $\phi_c \approx 4\%$ for calcite aggregates and Fontainebleau sandstone. Moreover, even though the porous microstructures in these rocks are quite different from sea ice, the permeability critical exponent in both cases falls into the lattice universality class. The permeability exponent of 3 for the hierarchical model is also about the same in both cases. It is interesting to note that a variation of four orders of magnitude in the permeability of calcite aggregates [55] is achieved with temperatures ranging from 633 K to 833 K, and with confining pressures from 200 MPa to 300 MPa. For sea ice, a similar variation in permeability occurs over a temperature range of about 15 K.

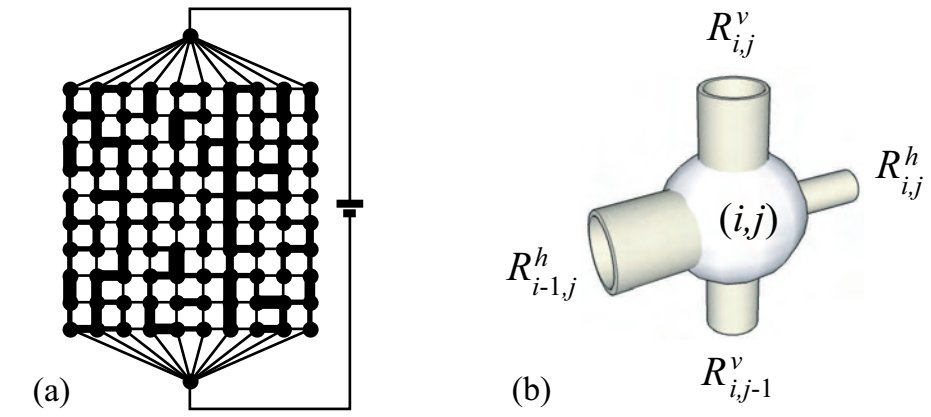

Figure 17: (a) Random pipe or resistor network. (b) Close-up of a node and adjoining ducts.

In [109] we developed a two dimensional random pipe network to simulate fluid flow through a porous medium, as illustrated in Figure 17. For sea ice the cross-sectional areas A of the pipes are chosen from the lognormal distribution in (10), with $\langle A(\phi)\rangle$ as before and $\rho^2 = 1$. The system is equivalent to a resistor network, which was solved using a fast multigrid method. While the model compared well with lab data for $\phi > 0.15$, it overestimated $k(\phi)$ for $\phi < 0.15$ where percolation effects, which were ignored, become significant. In accordance with our X-ray CT data, we introduced random *disconnections* so that the network falls apart as ϕ decreases. The results then agree well with the lab data, as shown in Figure 16 (b).

As discussed above, heat is exchanged between the ocean and atmosphere in the polar regions through sea ice. The thermal conductivity of sea ice is thus an important tranpsort coefficient entering into climate models. We will not discuss our work in this area, but simply mention that the methods for studying transport we have outlined here can be applied to bounding and numerically calculating this important sea ice parameter. One particularly interesting aspect of the thermal transport problem is that when brine flows through sea ice, such as for temperatures above the percolation threshold, there is an advective term in the heat equation. A velocity field helping to move heat around can enhance measured thermal conductivity, as has been

observed in Antarctic sea ice [60]. In conjunction with our fluid permeability work, we have been theoretically and numerically modeling such processes.

Sea Ice Remote Sensing: Assessing the Impact of Climate Change

Because of the global nature of monitoring earth's sea ice packs, information is usually obtained via remote sensing from platforms on satellites, aircraft and ships [87, 14, 104, 40, 39, 59]. The physics underlying the problem of remotely sensing sea ice concerns the interaction of electromagnetic waves with a polycrystalline composite of four components: pure ice, brine inclusions, air pockets, and solid salt deposits [100, 21]. Here we'll focus on the two main constituents in sea ice, namely, pure ice with brine inclusions. One of the grand challenges of sea ice remote sensing is to accurately recover the thickness distribution of the pack. Assessing the impact of global warming on the polar regions involves monitoring not only the ice extent, but the ice volume, which requires knowledge of ice thickness. While microwaves in the GHz frequency range have been commonly used in many applications, due to the absorbing nature of the brine phase and the short wavelengths involved, they typically can only penetrate into the upper portions of a sea ice floe. Lasers, such as on ICESat illustrated in Figure 18 (a), have been used to bounce off the ice or snow surface, and when compared with returns from the sea surface in open leads, can provide thickness estimates. Changes in ice sheet elevation in Antarctica and Greenland can also be similarly obtained.

Recently there has been increasing interest in using low frequency electromagnetic induction devices to estimate sea ice thickness [47, 45, 46, 106, 81, 80], as shown in Figure 18 (b). Electromagnetic fields in the MHz range, with wavelengths on the scale of meters are used to probe the air-ice-ocean interface and estimate the thickness of the ice layer. The technique relies on a time varying primary magnetic field (generated by a transmitter coil) inducing eddy currents in the seawater beneath the comparatively resistive ice. The secondary magnetic field produced is

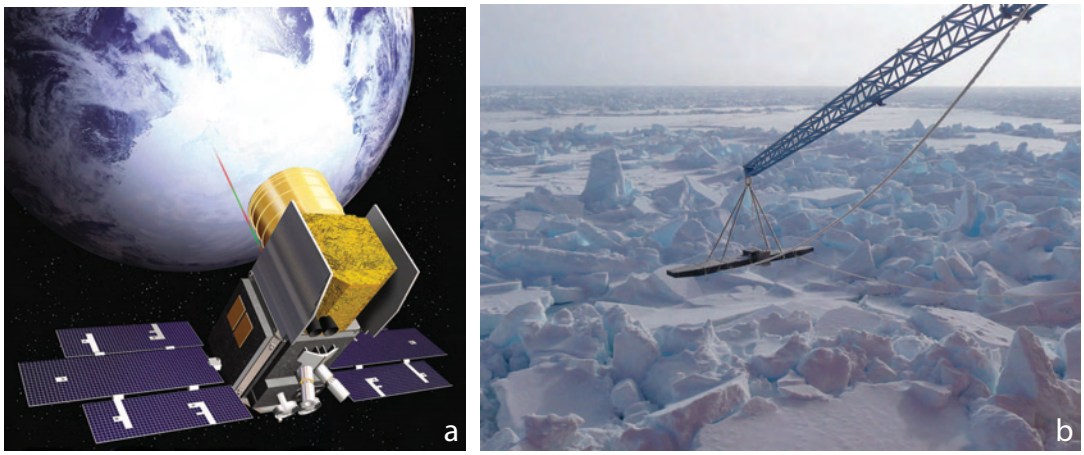

Figure 18: (a) NASA's Ice, Cloud and Land Elevation Satellite (ICESat) over Antarctica. It bounces laser pulses off the surfaces of ice sheets and sea ice to measure changes in thickness and monitor climate change. (b) An electromagnetic induction device for measuring sea ice thickness, called the "Worbot" after Australian sea ice scientist Tony Worby. It is mounted here on the icebreaker *Aurora Australis*, in the Antarctic sea ice pack, September 2007.

sensed by a receiver coil, determining an apparent conductivity which results essentially from an integration over the vertical distance between the instrument and induced currents. Accurate interpretation of the data relies on understanding how the conductivity of the sea ice, or more generally it complex permittivity, depends on the microstructural characteristics. For example, current methods of obtaining thickness estimates assume a single value for the conductivity. However, this key parameter can vary by over two orders of magnitude with depth throughout a given floe. Since typical sizes of the brine inclusions are on the submillimeter scale, the electromagnetic behavior of the sea ice can be treated using the quasistatic approximation, where the wavelength is much longer than the microstructural scale. Then the sea ice can be characterized electromagnetically via the effective complex permittivity tensor $\boldsymbol{\epsilon}^*$. There has been considerable work in the past on estimating and bounding $\boldsymbol{\epsilon}^*$ for sea ice, particularly in the microwave region [90, 98, 104, 37, 4, 88, 32, 35, 40]. We'll discuss here some of our work on bounding $\boldsymbol{\epsilon}^*$, particularly in this low frequency range, although the mathematics is quite general. We'll also discuss how we've been inverting these bounds and other information to recover microstructural

characteristics, which is important in monitoring fluid and thermal transport in sea ice. In this connection, there are new methods, such as cross-borehole tomography, which show promise in reconstructing the permittivity profile of sea ice, and in turn, the state of the ice itself [75, 51].

Here we review our work on theoretical bounds on the principal components of $\boldsymbol{\epsilon}^*$ with extensive outdoor tank and *in situ* data on $\boldsymbol{\epsilon}^*$ at 50 MHz, consisting of thousands of measurements, taken with a capacitance probe [44, 5]. In particular, we compare the low frequency measurements with the Bergman-Milton bounds [7, 66, 33] for the complex permittivity of a two phase composite with known constituent permittivities ϵ_1 and ϵ_2 and volume fractions p_1 and p_2. There are two types of these bounds which we employ. The first type assumes only the permittivity and volume fraction information, and are known as the complex elementary or arithmetic and harmonic mean bounds. The second type further assumes statistical isotropy in the composite microstructure, and are known as the complex Hashin-Shtrikman bounds [49].

All the data considered are situated well inside the complex elementary bounds. However, there are naturally occurring anisotropies in the brine microstructure, such as its preferred vertical orientation [100, 21], which become more pronounced above the critical brine volume fraction of about 5% where the brine phase percolates [38]. Also, preferred azimuthal alignment of the c-axes of individual crystals within the horizontal plane has long been observed in the Arctic [101], and was present in the Arctic sea ice whose permittivity was measured in one of the data sets considered here [5]. Preferred c-axis alignment is attended by anistropy in the brine microstructure, and anisotropic behavior of the complex permittivity within the horizontal plane [37]. Comparing the different data sets with the isotropic bounds yields interesting and useful insights about sea ice microstructure, its evolution with temperature, and its electromagnetic properties. We also invert the complex bounds to obtain rigorous estimates of the brine volume fraction from the permittivity data [18, 39, 63, 64].

Bounds on the complex permittivity of sea ice

Let us briefly describe the analytic continuation method for studying the effective properties of composite materials [7, 66, 33, 35]. Let the local complex permittivity $\epsilon(x)$ be a spatially stationary random field in $x \in \mathbb{R}^d$, for an appropriate probability space representing the set of realizations of the random medium. We assume $\epsilon(x)$ for 50 MHz takes the values $\epsilon_1 = 63.3 + i1930$ in brine and $\epsilon_2 = 3.06$ in ice [5], and write $\epsilon(x) = \epsilon_1\chi_1(x) + \epsilon_2\chi_2(x)$, where χ_j is the characteristic function of medium $j = 1, 2$, which equals one for all realizations having medium j at x, and equals zero otherwise. Let $E(x)$ and $D(x)$ be the stationary random electric and displacement fields satisfying the constitutive law $D(x) = \epsilon(x)E(x)$ and the equations

$$\nabla \times E(x) = 0, \qquad \nabla \cdot D(x) = 0, \tag{18}$$

with $\langle E(x) \rangle = e_k$, where e_k is a unit vector in the k^{th} direction for some $k = 1, \ldots, d$, and $\langle \cdot \rangle$ means an ensemble average or spatial average over all of $\mathbb{R}^d$.

The effective complex permittivity tensor $\boldsymbol{\epsilon}^*$ is defined by

$$\langle D \rangle = \boldsymbol{\epsilon}^* \langle E \rangle. \tag{19}$$

For simplicity, we focus on one diagonal coefficient $\epsilon^* = \epsilon^*_{kk}$. Due to the homogeneity of effective parameters, $\epsilon^*(\lambda\epsilon_1, \lambda\epsilon_2) = \lambda\epsilon^*(\epsilon_1, \epsilon_2)$, ϵ^* depends only on the ratio $h = \epsilon_1/\epsilon_2$, and we define $m(h) = \epsilon^*/\epsilon_2$. The two main properties of $m(h)$ are that it is analytic off $(-\infty, 0]$ in the h–plane, and that it maps the upper half plane to the upper half plane [6, 33], so that it is an example of a Herglotz, or Stieltjes function. The key step in the analytic continuation method is obtaining an integral representation for ϵ^*.

It is more convenient to work with the function [6] $F(s) = 1 - m(h)$, where $s = 1/(1-h)$, which is analytic off $[0, 1]$ in the s–plane. It was proven [33, 6] that $F(s)$ has the representation

$$F(s) = \int_0^1 \frac{d\mu(z)}{s - z}\,, \qquad s \notin [0, 1]\,, \tag{20}$$

where μ is a positive measure on $[0,1]$ (not to be confused with the viscosity from before). Formula (20) separates the parameter information in s from information about the mixture geometry contained in μ, a spectral measure of the operator $\Gamma\chi_1$, where $\Gamma = \nabla(-\Delta)^{-1}\nabla\cdot$. Statistical assumptions about the geometry are incorporated into μ via its moments $\mu_n = \int_0^1 z^n d\mu(z)$, which can be calculated from the correlation functions of the random medium, with $\mu_n = (-1)^n\langle\chi_1[(\Gamma\chi_1)^n e_k]\cdot e_k\rangle$. For the complex elementary bounds it is assumed that we know only $\mu_0 = p_1$, and if the medium is statistially isotropic we know $\mu_1 = p_1p_2/d$ as well.

Bounds on ϵ^*, or $F(s)$, are obtained by fixing s in (20), varying over admissible measures μ (or admissible geometries), such as those that satisfy only $\mu_0 = p_1$, and finding the corresponding range of values of $F(s)$ in the complex plane. Two types of bounds on ϵ^* are obtained. The first bound R_1 assumes only that the relative volume fractions p_1 and $p_2 = 1-p_1$ of the ice and brine are known, with $\mu_0 = p_1$ satisfied. In this case, the admissible set of measures forms a compact, convex set $\mathcal{M}_0$. Since (20) is a linear functional of μ, the extreme values of F are attained by extreme points of $\mathcal{M}_0$, which are the Dirac point measures $p_1\delta_z$. The values of F lie inside the region R_1 bounded by circular arcs, one of which is parameterized in the F–plane by

$$C_1(z) = \frac{p_1}{s-z}\ , \qquad 0 \le z \le p_2. \tag{21}$$

To display the other arc, we use the auxiliary function [8] $E(s) = 1 - \epsilon_1/\epsilon^*$, which is a Herglotz function like $F(s)$, analytic off $[0,1]$. Then in the E–plane, we can parameterize the other circular boundary of R_1 by

$$\hat{C}_1(z) = \frac{p_2}{s-z}\ , \qquad 0 \le z \le p_1. \tag{22}$$

In the common ϵ^*–plane, R_1 has vertices $V_1 = \epsilon_1/(1-\hat{C}_1(0)) = (p_1/\epsilon_1 + p_2/\epsilon_2)^{-1}$ and $W_1 = \epsilon_2(1-C_1(0)) = p_1\epsilon_1 + p_2\epsilon_2$. This region collapses to the interval $(p_1/\epsilon_1 + p_2/\epsilon_2)^{-1} \le \epsilon^* \le p_1\epsilon_1 + p_2\epsilon_2$ when ϵ_1 and ϵ_2 are real, which are the arithmetic (upper) and harmonic (lower) mean bounds. The complex elementary bounds (21) and (22) are optimal and can be attained

by coated ellipsoidal geometries as the aspect ratio varies.

If the material is further assumed to be statistically isotropic, i.e., $\epsilon^*_{ik} = \epsilon^* \delta_{ik}$, then $\mu_1 = p_1 p_2/d$ must be satisfied as well. A convenient way of including this information [8] is to use the function $F_1(s) = 1/p_1 - 1/(sF(s))$, which is, again, a Herglotz function with a representation similar to (20) with a measure μ^1. The constraint $\mu_1 = p_1 p_2/d$ on $F(s)$ is then transformed to a restriction of only the mass, or zeroth moment μ^1_0 of μ^1, with $\mu^1_0 = p_2/p_1 d$. Applying the same procedure as for R_1 yields a region R_2, whose boundaries are again circular arcs. In the F–plane, one of these arcs is parameterized by

$$C_2(z) = \frac{p_1(s-z)}{s(s-z-p_2/d)}\,, \qquad 0 \le z \le (d-1)/d. \tag{23}$$

In the E–plane, the other arc is parameterized by

$$\hat{C}_2(z) = \frac{p_2(s-z)}{s(s-z-p_1(d-1)/d)}\,, \qquad 0 \le z \le 1/d. \tag{24}$$

In the ϵ^*–plane, R_2 has vertices $V_2 = \epsilon_2(1 - C_2(0))$ and $W_2 = \epsilon_1/(1 - \hat{C}_2(0))$, and collapses to the interval

$$\epsilon_2 + p_1 \Big/ \left(\frac{1}{\epsilon_1 - \epsilon_2} + \frac{p_2}{d\epsilon_2}\right) \le \epsilon^* \le \epsilon_1 + p_2 \Big/ \left(\frac{1}{\epsilon_2 - \epsilon_1} + \frac{p_1}{d\epsilon_1}\right), \tag{25}$$

when ϵ_1 and ϵ_2 are real with $\epsilon_1 \ge \epsilon_2$, which are the Hashin–Shtrikman bounds [49]. When $\epsilon_1 \le \epsilon_2$, the sequence of inequalities is reversed. The vertices V_2 and W_2 (which correspond to the expressions in (25)), are attained by the Hashin–Shtrikman coated sphere geometries. Extensions of the analytic continuation method and bounds to multicomponent media involve techniques of several complex variables [34, 29, 68, 67, 20].

Now we compare three extensive sets of data [5] on the complex permittivity of sea ice with the forward and inverse bounds. Measurements were taken in land-fast ice in the Chukchi Sea near Barrow, Alaska (14,004 data points) and in McMurdo Sound, Antarctica (2,382 data points) and in artificial, young sea ice in an outdoor tank in Fairbanks, Alaska (6,403 data

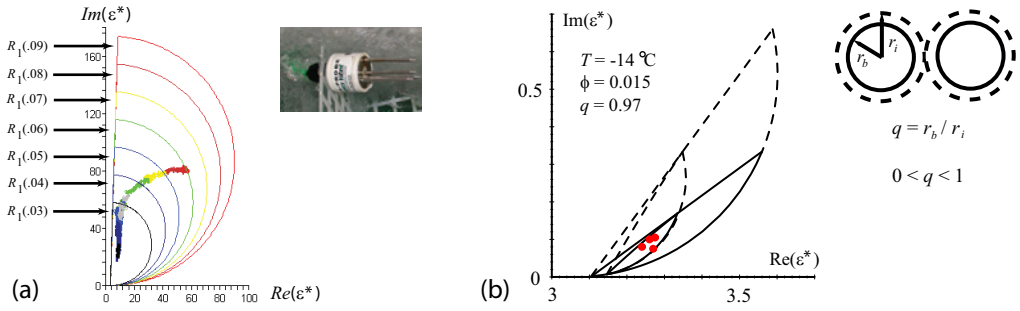

Figure 19: (a) Comparison of data on the complex permittivity at 50 MHz of sea ice grown in an ice tank with the elementary bounds. Data in a brine porosity interval signified by a given color lies inside the region of the same color. The data colored grey have porosities in the interval $[0.049, 0.051]$. The capacitance probe is shown on the right. (b) Matrix-particle bounds on ϵ^* (solid curves), along with the complex elementary and Hashin-Shtrikman bounds (dotted curves), compared with 4.75 GHz data in red.

points). The permittivity was measured by deploying an array of Stevens Water Monitoring Systems Hydraprobes. Each Hydraprobe is a coaxial probe with a central tine surrounded by three equally spaced outer tines, aligned horizontally, as shown in the photo inset in Figure 19 (a). The three outer tines are held at ground potential, and a voltage is applied to the central tine at 50 MHz frequency, resulting in a circularly polarized wave with electric field predominantly in the plane perpendicular to the tines. The complex permittivity measured by the probe represents an average of the components of $\boldsymbol{\epsilon}^*$ in this plane.

In Figure 19 (a) the full data set for the Fairbanks ice tank experiment is displayed along with a series of regions $R_1(\phi)$, for the indicated values of the brine porosity ϕ. The data has been grouped into intervals of porosity, $[0.02, 0.03]$, $[0.03, 0.04]$, ..., $[0.08, 0.09]$, with a different color for each interval. The corresponding elementary bound has the same color. All the data in each interval lie inside the corresponding bound. The data marked with the grey color lies in the porosity interval $[0.049, 0.051]$, which corresponds to the percolation threshold of about 5% conjectured in [38].

It is useful to note that tighter bounds [35, 40] on ϵ^* can be obtained if the material is

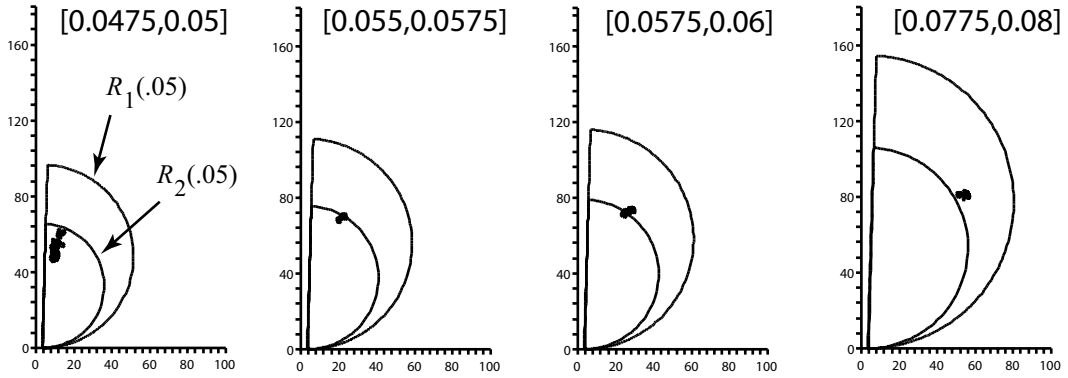

Figure 20: Comparison of ice tank data on the complex permittivity of sea ice at 50 MHz with the elementary and isotropic bounds. The isotropic bounds are violated as brine volume increases in this case.

known to have a matrix-particle structure with separated inclusions, like sea ice at temperatures colder than its critical temperature. In this case, the support of μ lies in an interval $[s_m, s_M]$, $0 < s_m < s_M < 1$ [13]. The more separated the inclusions, the smaller the support interval, and the tighter the bounds. Comparison of higher frequency 4.75 GHz data (red dots) on the complex permittivity ϵ^* of sea ice for $\epsilon_1 = 51 + i45$ and $\epsilon_2 = 3.1$, with a series of bounds [35] is shown in Figure 19 (b). The outer dotted curves are complex arithmetic and harmonic mean bounds, and the inner curves are Hashin-Shtrikman bounds. The solid bounds are matrix-particle versions. The parameter q measures the separation of inclusions, and can be bounded using permittivity data [70].

In Figure 20 we display a series of comparisons of the 50 MHz data in the porosity intervals shown, with corresponding elementary bounds $R_1(\phi_{max})$ and the isotropic bounds $R_2(\phi_{max})$, where ϕ_{max} is the largest porosity in each interval. The development of anisotropy in the dielectric measurements, or violation of the isotropic bounds, as brine volume increases through 5%, is consistent with an increasingly connected and vertically elongated brine microstructure. This behavior in the data would likely be accentuated if the electric field were oriented predominantly in the vertical direction.

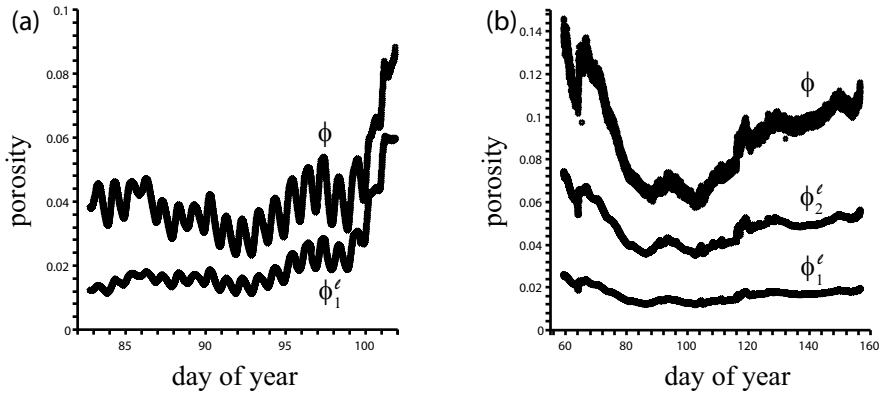

Figure 21: Comparison of the actual brine porosity ϕ with time to the inverse lower bounds, for the ice tank data in (a) and for the Barrow data in (b).

Inverse bounds for structural parameters

The objective of inverse bounds is to use data about the electromagnetic response of sea ice to recover information about its structural parameters, in particular its brine volume fraction $p_1 = \phi$, or porosity. As mentioned above, the porosity ϕ can be written as a function of the bulk ice salinity S and temperature T, as derived by semi-empirical approaches from the sea ice phase relations [100, 21]. Given salinity information, for example, inverting for porosity yields temperature information. The inverse method [18, 39, 63, 64] we use here yields intervals of uncertainty for the brine volume fraction ϕ. Given an observed value of the complex permittivity ϵ^*, ϕ is increased until the value of ϵ^* touches one boundary of the region R_1 described in the previous section, and is then decreased until the value touches the other boundary. This procedure gives a range of values $\phi_1^\ell \leq \phi \leq \phi_1^u$, with

$$\phi_1^\ell = |f|^2 \frac{Im(\overline{s})}{Im(f)} \,, \qquad \phi_1^u = 1 - \frac{|g|^2 Im(\overline{t})}{Im(g)} \,, \tag{26}$$

where f is the known value of $F(s)$ and g is the known value of $G(t) = 1 - \epsilon^*/\epsilon_1$ with $t = 1 - s$. If the material is further assumed to be statistically isotropic, second order inverse bounds $\phi_2^\ell \leq \phi \leq \phi_2^u$ can be obtained. Formulas for ϕ_2^ℓ and ϕ_2^u are found in [18]. We mention that E. Cherkaev has made recent progress on developing more sophisticated methods for reconstructing

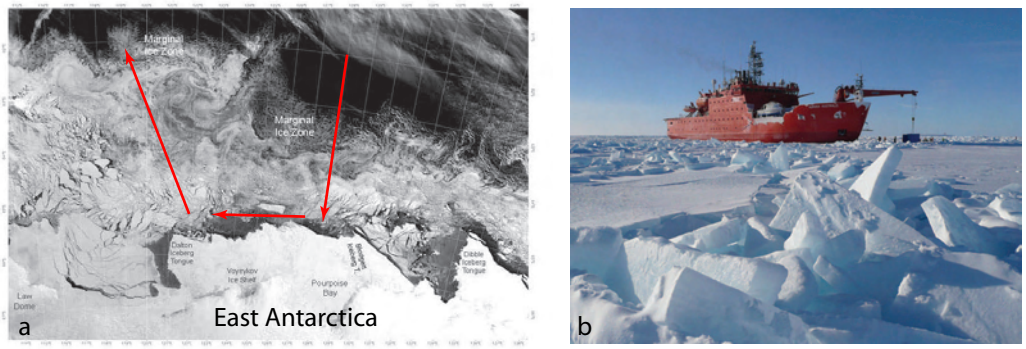

Figure 22: (a) Satellite image of the region off the coast of East Antarctica where the SIPEX expedition took place. The red arrows roughly indicate the ship track of the Australian icebreaker *Aurora Australis*, shown in (b).

the spectral measure μ of the composite microgeometry from measurements of the effective complex permittivity [16, 17, 108, 107]. Such methods will likely be useful in obtaining more detailed information about sea ice microstructure, as they have been for bone microstructure, and in monitoring osteoporosis [10].

In Figure 21 (a), the actual brine porosity $\phi(t)$ as a function of time t for the ice tank experiment is compared with the lower inverse bound ϕ_1^ℓ. Due to the high contrast in the materials, the corresponding upper bound is quite large and currently provides little information. We see that the actual data lies above the lower bound, and that the variations in the reconstructed lower bound follow the variations in the actual porosity. In Figure 21 (b), the actual brine porosity for the Barrow data is compared with the lower inverse bounds ϕ_1^ℓ and ϕ_2^ℓ. The inverse bounds are obeyed, and the variations in $\phi(t)$ are reflected in the reconstructions.

Measurements of fluid and electrical transport in Antarctic sea ice

During September and October of 2007, University of Utah math student Adam Gully and the author participated in a six week voyage into the Antarctic sea ice pack. The Sea Ice Physics and Ecosystem eXperiment (SIPEX), conducted off the coast of East Antarcica, as shown in Figure

22, was a major component of Australia's project contributions to the worldwide International Polar Year activities of 2007-2008. An extensive science program conducted by 45 scientists from 10 nations was led jointly by the Antarctic Climate & Ecosystems Cooperative Research Centre (ACE CRC) and the Australian Antarctic Division. Valuable information was obtained that will help develop more accurate global climate models and will also help us understand how polar ecosystems might respond to future climate change.

Researchers employed a suite of cutting-edge technologies, including airborne laser altimetry and radar, and an under-ice remotely operated vehicle (ROV). For the first time ever in Antarctica, helicopter flights covered thousands of kilometres tracking over the sea ice, gathering large-scale information about the height of the snow and ice surfaces above sea level. The helicopter data were complemented by information gathered from ice coring and other work directly on the ice. The combined information will help validate satellite altimetry data, which will eventually be used to monitor changes in sea ice thickness around Antarctica.

Biologists combined classical ice coring techniques with the ROV to study the underside of the sea ice, to map the distribution of sea ice algae. The ROV observations showed high concentrations of Antarctic krill living on the underside of the sea ice as well as in cracks between ice floes. Other scientists worked on ice algae physiology and sea ice biogeochemistry to better understand processes in the Antarctic sea ice zone during the transition from winter to summer. Oceanographers studied the water mass properties and currents beneath the sea ice and found that, contrary to what was expected, the patterns of sea ice drift appear to be affected more by ocean currents than by wind.

The author and Gully conducted field studies of the fluid and electrical transport properties of first year sea ice, in conjunction with our mathematical modeling work. We made the first fluid permeability measurements of Antarctic pack ice, and conducted fluid tracer experiments on extracted blocks of sea ice. In close connection with these fluid measurements, we used

Figure 23: The author taking a sea ice core in (a), and making a permeability measurement in (b), by measuring the rate at which sea water fills in the partial hole through the ice. (c) Sea water is just about to flood the surface through the permeability hole. (d) The Wenner array for surface impedance tomography used to reconstruct the conductivity profile of sea ice. (e) Adam Gully (right) sets up a Wenner array, while Kazu Tateyama takes thickness measurements with an EM induction instrument. (f) The Wenner array adapted to take direct measurements of the vertical conductivity of extracted sea ice cores.

Figure 24: Antarctica is not only of great scientific interest, but is a place of unique beauty and adventure.

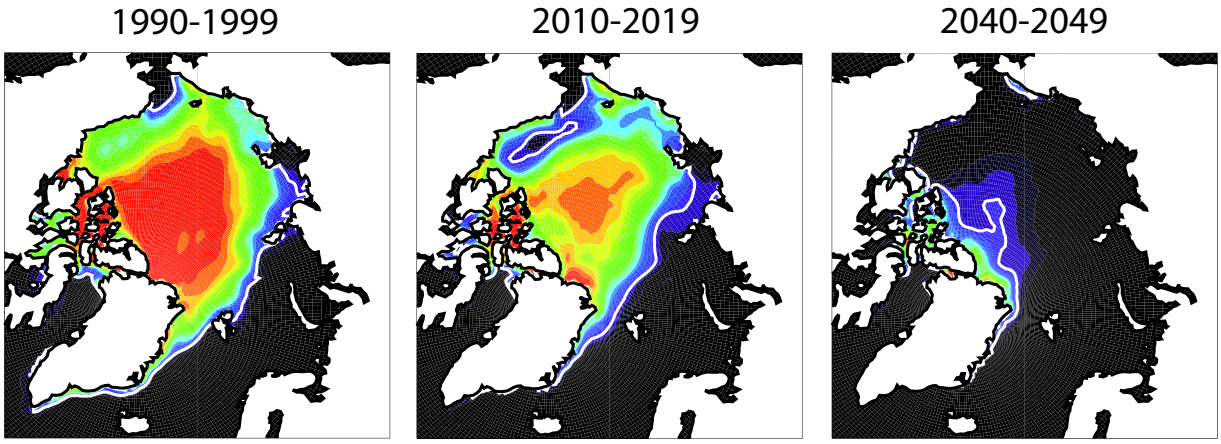

Figure 25: Coupled climate model simulations from the Community Climate System Model, version 3, showing September sea ice concentration averaged for three different time periods (left to right) 1990-1999, 2010-2019, and 2040-2049. The white line indicates the simulated ice extent, defined as the 15% ice concentration contour. This and other similar climate models suggest significant sea ice loss will occur over the next 50 years, and near ice-free September conditions may be reached in the Arctic by the mid-21st century. Some scientists predict such a decline over an even shorter period of time. (Courtesy of Marika Holland)

surface impedance tomography via a Wenner electrode array to reconstruct the conductivity profile of the ice. We also modified our Wenner configuration to directly measure the vertical conductivity component of extracted cores - a first for sea ice. These measurements will allow the fluid permeability data to be directly related to sea ice electrical properties. Our electrical work, joint with voyage leader Tony Worby, was done in the same exact locations and configurations as EM induction thickness measurements conducted by Japanese sea ice scientist Kazu Tateyama for later correlation. We are still in the process of analyzing the data and preparing it for publication, so our results will be presented elsewhere.

Conclusions and future challenges in sea ice modeling

Numerous challenges remain in the modeling of sea ice for climate applications. Many important processes are only crudely represented, such as snow-ice formation, albedo evolution, aspects of the snow pack overlying the ice cover, and the parameterization of ice strength and dynamic-

driven ice ridging and rafting. Figure 25 shows dire model predictions for the decline of the summer Arctic sea ice pack, and much work remains to refine these predictions based on our increasing knowledge of important processes in sea ice, and how the pack interacts with the ocean and atmosphere.

Our work on fluid transport is central to a broad range of problems in the geophysics and biology of sea ice, yet fundamental studies have been lacking. We have developed a unified theory of the fluid permeability of sea ice and its dependence on microstructural evolution with temperature. The theory ties together different approaches to estimating effective composite behavior, and closely captures laboratory and Arctic field data. We have also made progress in CT imaging of sea-ice microstructure, quantifying the thermal evolution of pore connectivity and morphology at the (sub)granular scale, which in turn has informed the theoretical advances. Our work on sea ice electrical properties helps provides a theoretical basis for new techniques in remote sensing, in particular those which help to monitor the impact of climate change.

Our work demonstrates how to link information about the micro-scale structure to macroscopic transport properties, which in turn constrain global-scale processes of climatological and biological importance. The results yield simple parameterizations of fluid transport through sea ice in terms of of porosity ϕ, and therefore the state variables T and S, and can help to improve the representation of sea ice in climate, biogeochemical and geophysical models. Future studies will have to examine how these findings impact the simulation of heat and fluid flow through sea ice in large-scale models, which currently oversimplify such processses.

Acknowledgements: We thank Hajo Eicken, Daniel Pringle, Jingyi Zhu, Amy Heaton, Adam Gully, Megan Morris, Ali Jabini, Christian Sampson, Lars Backstrom, Jeremy Miner, Tony Worby, and James Reid for their collaboration on the work reviewed here. We would also like to thank Donald Perovich, Marika Holland, Steve Ackley, Elizabeth Hunke, and Cecilia Bitz,

for helpful discussions and input, and for providing some of the figures shown here. We are grateful for the support provided by the Division of Atmospheric Sciences and the Division of Mathematical Sciences at the US National Science Foundation (NSF), through Grant DAS-0222171 in the Collaboration in Mathematical Geosciences (CMG) Program, and Grant DMS-0537015. A number of the students involved in the research presented here were supported by the NSF Research Experiences for Undergraduates (REU) Program, as well as an NSF VIGRE grant to the University of Utah Math Department, and we thank NSF for the unique opportunities it has made possible for these students. In addition to supporting Gully's travel to Antarctica, six undergraduates have particpated in trips to the Arctic for their work on sea ice with the author, for which they are grateful. Part of the work presented was also supported by a grant of High Perfomance Computing (HPC) resources from the Arctic Region Supercomputing Center at the University of Alaska Fairbanks, and we thank them as well.

To find out more: If you are interested in finding out more about math and sea ice, you can visit the author's web page www.math.utah.edu/∼golden. There you will also be able to link to a video on the SIPEX expedition to Antarctica produced by the author, located under www.math.utah.edu/∼golden/media.html. If you are interested in learning about how math is being used to address the big questions in climate science (including more about sea ice), you are encouraged to visit the Math Awareness Month 2009 website at www.mathaware.org on "Mathematics and Climate."

References

[1] S. F. Ackley, V. I. Lytle, K. M. Golden, M. N. Darling, and G. A. Kuehn. Sea ice measurements during ANZFLUX. *Antarctic J. U. S.*, 30:133–135, 1995.

[2] G. Allaire. Homogenization and two-scale convergence. *SIAM J. Math. Anal.*, 23:261–298,

1992.

[3] G. Allaire. One-phase Newtonian flow. In U. Hornung, editor, *Homogenization and Porous Media*, pages 45–68. Springer – Verlag, 1997.

[4] S. A. Arcone, A. J Gow, and S. McGrew. Structure and dielectric properties at 4.8 and 9.5 GHz of saline ice. *J. Geophys. Res.*, 91(C12):14281–14303, 1986.

[5] L. G. E. Backstrom and H. Eicken. Capacitance probe measurements of brine volume and bulk salinity in first-year sea ice. *Cold Reg. Sci. Tech.*, 46:167–180, 2006.

[6] D. J. Bergman. The dielectric constant of a composite material – A problem in classical physics. *Phys. Rep. C*, 43(9):377–407, 1978.

[7] D. J. Bergman. Exactly solvable microscopic geometries and rigorous bounds for the complex dielectric constant of a two-component composite material. *Phys. Rev. Lett.*, 44:1285, 1980.

[8] D. J. Bergman. Rigorous bounds for the complex dielectric constant of a two–component composite. *Ann. Phys.*, 138:78, 1982.

[9] B. Berkowitz and I. Balberg. Percolation approach to the problem of hydraulic conductvity in porous media. *Transport in Porous Media*, 9:275–286, 1992.

[10] C. Bonifasi-Lista and E. Cherkaev. Identification of bone microstructure from effective complex modulus. In E. Inan and A. Kiris, editors, *Vibration Problems*, volume 111, pages 91–96. Springer Proceedings in Physics, 2005.

[11] T. Bourbie and B. Zinszner. Hydraulic and acoustic properties as a function of porosity in Fontainebleau sandstone. *J. Geophys. Res.*, 90(B13):11,524–11,532, 1985.

[12] S. R. Broadbent and J. M. Hammersley. Percolation processes I. Crystals and mazes. *Proc. Cambridge Philos. Soc.*, 53:629–641, 1957.

[13] O. Bruno. The effective conductivity of strongly heterogeneous composites. *Proc. R. Soc. London A*, 433:353–381, 1991.

[14] F. D. Carsey, editor. *Microwave Remote Sensing of Sea Ice, Geophysical Monograph 68*. American Geophysical Union, Washington D.C., 1992.

[15] J. T. Chayes and L. Chayes. Bulk transport properties and exponent inequalities for random resistor and flow networks. *Comm. Math. Phys.*, 105:133–152, 1986.

[16] E. Cherkaev. Inverse homogenization for evaluation of effective properties of a mixture. *Inverse Problems*, 17:1203–1218, 2001.

[17] E. Cherkaev. Inverse homogenization with diagonal Padé approximants. *ICIAM07-Proceedings: Proceedings in Applied Mathematics and Mechanics (PAMM)*, 7(1), 2007.

[18] E. Cherkaeva and K. M. Golden. Inverse bounds for microstructural parameters of composite media derived from complex permittivity measurements. *Waves in Random Media*, 8(4):437–450, 1998.

[19] G. F. N. Cox and W. F. Weeks. Brine drainage and initial salt entrapment in sodium chloride ice. Research Report 354, USA CRREL, Hanover, NH, 1975.

[20] G. F. Dell'Antonio and V. Nesi. A general representation for the effective dielectric constant of a composite. *J. Math. Phys.*, 29:2688, 1988.

[21] H. Eicken. Growth, microstructure and properties of sea ice. In D. N. Thomas and G. S. Dieckmann, editors, *Sea Ice: An Introduction to its Physics, Chemistry, Biology and Geology*, pages 22–81. Blackwell, Oxford, 2003.

[22] H. Eicken, T. C. Grenfell, D. K. Perovich, J. A. Richter-Menge, and K. Frey. Hydraulic controls of summer Arctic pack ice albedo. *J. Geophys. Res. (Oceans)*, 109(C18):C08007.1–C08007.12, 2004.

[23] J. Freitag. The hydraulic properties of Arctic sea ice - Implications for the small-scale particle transport. *Ber. Polarforsch.*, 325:150 pp., 1999. (in German).

[24] J. Freitag and H. Eicken. Meltwater circulation and permeability of Arctic summer sea ice derived from hydrological field experiments. *J. Glaciol.*, 49:349–358, 2003.

[25] A. P. Friedman and N. A. Seaton. Critical path analysis of the relationship between permeability and electrical conductivity of three-dimensional pore networks. *Water Resources Res.*, 34(7):1703–1710, 1998.

[26] C. H. Fritsen, V. I. Lytle, S. F. Ackley, and C. W. Sullivan. Autumn bloom of Antarctic pack-ice algae. *Science*, 266:782–784, 1994.

[27] R. Glantz and M. Hilpert. Invasion percolation through minimum weight spanning trees. 2008. preprint.

[28] R. Glantz and M. Hilpert. Tight dual models of pore spaces. *Adv. Water Res.*, 2008. In press, doi: 10.1016/j.advwatres.2008.01.015 S0309-1708(08)00019-5.

[29] K. Golden. Bounds on the complex permittivity of a multicomponent material. *J. Mech. Phys. Solids*, 34(4):333–358, 1986.

[30] K. Golden. Convexity and exponent inequalities for conduction near percolation. *Phys. Rev. Lett.*, 65(24):2923–2926, 1990.

[31] K. Golden. Exponent inequalities for the bulk conductivity of a hierarchical model. *Comm. Math. Phys.*, 43(3):467–499, 1992.

[32] K. Golden. Bounds on the complex permittivity of sea ice. *J. Geophys. Res. (Oceans)*, 100(C7):13,699 – 13,711, 1995.

[33] K. Golden and G. Papanicolaou. Bounds for effective parameters of heterogeneous media by analytic continuation. *Comm. Math. Phys.*, 90:473–491, 1983.

[34] K. Golden and G. Papanicolaou. Bounds for effective parameters of multicomponent media by analytic continuation. *J. Stat. Phys.*, 40(5/6):655–667, 1985.

[35] K. M. Golden. The interaction of microwaves with sea ice. In G. Papanicolaou, editor, *Wave Propagation in Complex Media, IMA Volumes in Mathematics and its Applications, Vol. 96*, pages 75 – 94. Springer – Verlag, 1997.

[36] K. M. Golden. Percolation models for porous media. In U. Hornung, editor, *Homogenization and Porous Media*, pages 27 – 43. Springer – Verlag, 1997.

[37] K. M. Golden and S. F. Ackley. Modeling of anisotropic electromagnetic reflection from sea ice. *J. Geophys. Res. (Oceans)*, 86(C9):8107–8116, 1981.

[38] K. M. Golden, S. F. Ackley, and V. I. Lytle. The percolation phase transition in sea ice. *Science*, 282:2238–2241, 1998.

[39] K. M. Golden, D. Borup, M. Cheney, E. Cherkaeva, M. S. Dawson, K. H. Ding, A. K. Fung, D. Isaacson, S. A. Johnson, , A. K. Jordan, J. A. Kong, R. Kwok, S. V. Nghiem, R. G. Onstott, J. Sylvester, D. P. Winebrenner, and I. Zabel. Inverse electromagnetic scattering models for sea ice. *IEEE Trans. Geosci. Rem. Sens.*, 36(5):1675–1704, 1998.

[40] K. M. Golden, M. Cheney, K. H. Ding, A. K. Fung, T. C. Grenfell, D. Isaacson, J. A. Kong, S. V. Nghiem, J. Sylvester, and D. P. Winebrenner. Forward electromagnetic scattering models for sea ice. *IEEE Trans. Geosci. Rem. Sens.*, 36(5):1655–1674, 1998.

[41] K. M. Golden, H. Eicken, A. L. Heaton, J. Miner, D. Pringle, and J. Zhu. Thermal evolution of permeability and microstructure in sea ice. *Geophys. Res. Lett.*, 34:L16501 (6 pages and issue cover), doi:10.1029/2007GL030447, 2007.

[42] K. M. Golden, A. L. Heaton, H. Eicken, and V. I. Lytle. Void bounds for fluid transport in sea ice. *Mechanics of Materials*, 38:801–817, 2006.

[43] K. M. Golden and S. M. Kozlov. Critical path analysis of transport in highly disordered random media. In V. Berdichevsky, V. Jikov, and G. Papanicolaou, editors, *Homogenization: Serguei Kozlov Memorial Volume*, pages 21 – 34. World Scientific, 1999.

[44] A. Gully, L. G. E. Backstrom, H. Eicken, and K. M. Golden. Complex bounds and microstructural recovery from measurements of sea ice permittivity. *Physica B*, 394:357–362, 2007.

[45] C. Haas. Evaluation of ship-based electromagnetic-inductive thickness measurements of summer sea-ice in the Bellingshausen and Amundsen Seas, Antarctica. *Cold Reg. Sci. Tech.*, 27:1–16, 1998.

[46] C. Haas. Late-summer sea ice thickness variability in the Arctic Transpolar Drift 1991-2001 derived from ground-based electromagnetic sounding. *Geophys. Res. Lett.*, 31:L09402, 2004. doi:10.1029/2003GL019394.

[47] C. Haas, S. Gerland, H. Eicken, and H. Miller. Comparison of sea-ice thickness measurements under summer and winter conditions in the Arctic using a small electromagnetic induction device. *Geophysics*, 62:749757, 1997.

[48] B. I. Halperin, S. Feng, and P. N. Sen. Differences between lattice and continuum percolation transport exponents. *Phys. Rev. Lett.*, 54(22):2391–2394, 1985.

[49] Z. Hashin and S. Shtrikman. A variational approach to the theory of effective magnetic permeability of multiphase materials. *J. Appl. Phys.*, 33:3125–3131, 1962.

[50] U. Hornung (Ed.). *Homogenization and Porous Media*. Springer, New York, 1997.

[51] M. Ingham, D. J. Pringle, and H. Eicken. Cross-borehole resistivity tomography of sea ice. *Cold Reg. Sci. Technol.*, 52:263–277, 2008. 10.1016/jcoldregions.2007.05.002.

[52] P. D. Jackson, D. T. Smith, and P. N. Stanford. Resistivity-porosity-particle shape relationships for marine sands. *Geophysics*, 43:1250–1268, 1978.

[53] M. O. Jeffries, editor. *Antarctic Sea Ice: Physical processes, interactions and variability*. American Geophysical Union, Washington D.C., 1998.

[54] J. B. Keller. Darcy's law for flow in porous media and the two-space method. In R. L. Sternberg, editor, *Nonlinear Partial Differential Equations in Engineering and Applied Sciences*, pages 429–443. Dekker, 1980.

[55] M. A. Knackstedt and S. F. Cox. Percolation and pore geometry of crustal rocks. *Phys. Rev. E*, 51(6A):R5181–R5184, 1995.

[56] R. P. Kusy and D. T. Turner. Electrical resistivity of a polymeric insulator containing segregated metallic particles. *Nature*, 229:58–59, 1971.

[57] W. B. Lindquist and A. Venkatarangan. Investigating 3d geometry of porous media from high resolution images. *Phys. Chem. Earth*, A25:593–599, 1999.

[58] W. B. Lindquist, A. Venkatarangan, J. Dunsmuir, and T.-F. Wong. Pore and throat size distributions measured from synchrotron x-ray tomographic images of fontainbleau sandstones. *J. Geopyhs. Res.*, 105B:21508–21528, 2000.

[59] D. Lubin and R. Massom. *Polar Remote Sensing, Volume I: Atmosphere and Oceans.* Springer Verlag, New York, 2006.

[60] V. I. Lytle and S. F. Ackley. Heat flux through sea ice in the Western Weddell Sea: Convective and conductive transfer processes. *J. Geophys. Res.*, 101(C4):8853–8868, 1996.

[61] T. Maksym and M. O. Jeffries. Phase and compositional evolution of the flooded layer during snow-ice formation of Antarctic sea ice. *Ann. Glac.*, 33:37–44, 2001.

[62] J. A. Maslanik, C. Fowler, J. Stroeve, S. Drobot, J. Zwally, D. Yi, and W. Emery. A younger, thinner Arctic ice cover: Increased potential for rapid, extensive sea-ice loss. *Geophys. Res. Lett.*, 34:L24501, doi:10.1029/2007GL032043, 2007.

[63] R. C. McPhedran, D. R. McKenzie, and G. W. Milton. Extraction of structural information from measured transport properties of composites. *Appl. Phys. A*, 29:19–27, 1982.

[64] R. C. McPhedran and G. W. Milton. Inverse transport problems for composite media. *Mat. Res. Soc. Symp. Proc.*, 195:257–274, 1990.

[65] M. G. McPhee, S. F. Ackley, P. Guest, B. A. Huber, D. G. Martinson, J. H. Morison, R. D. Muench, L. Padman, and T. P. Stanton. The Antarctic Zone Flux Experiment. *Bull. Amer. Met. Soc.*, 77:1221–1232, 1996.

[66] G. W. Milton. Bounds on the complex dielectric constant of a composite material. *Appl. Phys. Lett.*, 37:300–302, 1980.

[67] G. W. Milton. Multicomponent composites, electrical networks and new types of continued fractions I, II. *Comm. Math. Phys.*, 111:281–327, 329–372, 1987.

[68] G. W. Milton and K. Golden. Representations for the conductivity functions of multicomponent composites. *Comm. Pure. Appl. Math.*, 43:647, 1990.

[69] N. Ono and T. Kasai. Surface layer salinity of young sea ice. *Ann. Glaciol.*, 6:298–299, 1985.

[70] C. Orum, E. Cherkaev, and K. M. Golden. Inverse bounds on the separation of inclusions in a composite from effective property measurements. In preparation.

[71] D. K. Perovich and A. J. Gow. A quantitative description of sea ice inclusions. *J. Geophys. Res.*, 101(C8):18,327–18,343, 1996.

[72] D. K. Perovich, J. A. Richter-Menge, K. F. Jones, and B. Light. Sunlight, water, and ice: Extreme Arctic sea ice melt during the summer of 2007. *Geophys. Res. Lett.*, 35:L11501, 2008. doi:10.1029/2008GL034007.

[73] C. Petrich, P. J. Langhorne, and Z. F. Sun. Modelling the interrelationships between permeability, effective porosity and total porosity in sea ice. *Cold Reg. Sci. Tech.*, 44(2):131–144, 2006.

[74] D. C. Powell and T. Markus. Effects of snow depth forcing on Southern Ocean sea ice simulations. *J. Geophys. Res. C (Oceans)*, 110:C06001, doi:10.1029/2003JC002212, 2005.

[75] D. J. Pringle, M. Ingham, H. Eicken, G. Dubuis, and L. Backstrom. Tracking the evolution of sea ice properties with in-situ dielectric probes and cross-borehole resistivity tomography. *Eos Trans. AGU*, 88(52), 2007. Fall Meet. Suppl., Abstract NS11A-0157.

[76] D. J. Pringle, J. E. Miner, and H. Eicken. Temperature-dependent microstructure of sea ice single crystals from x-ray computed tomography. In preparation, 2008.

[77] D. J. Pringle, J. E. Miner, H. Eicken, and K. M. Golden. Pore-space percolation in sea ice single crystals. Submitted, October, 2008.

[78] D. J. Pringle, J. E. Miner, R. Glantz, M. Hilpert, and H. Eicken. Temperature-dependent pore space of sea ice: X-ray computed tomography and dual model network analysis. *Eos Trans. AGU*, 87(52), 2006. Fall Meet. Suppl., Abstract H51F-0545.

[79] M. Prodanovic, W. B. Lindquist, and R. S. Seright. 3D image-based characterization of fluid displacement in a Berea core. *Adv. Water Res.*, 30(2):214–226, 2007.

[80] J. E. Reid, A. Pfaffling, A. P. Worby, and J. R. Bishop. In situ measurements of the direct-current conductivity of Antarctic sea ice: implications for airborne electromagnetic sounding of sea-ice thickness. *Ann. Glaciol.*, 44:217–223, 2006.

[81] J. E. Reid, A. P. Worby, J. Vrbancich, and A. I. S. Munro. Shipborne electromagnetic measurements of Antarctic sea-ice thickness. *Geophysics*, 68(5):1537–1546, 2003.

[82] J. Richter-Menge, J. Comiso, W. Meier, S. Nghiem, and D. Perovich. Sea ice cover. *Arctic Report Card*, 2008. National Oceanic and Atmospheric Administration, www.arctic.noaa.gov/reportcard/seaice.html.

[83] J. Rubinstein and S. Torquato. Flow in random porous media: Mathematical formulation variational principles, and rigorous bounds. *J. Fluid Mech.*, 206, 1989.

[84] M. Sahimi. *Flow and Transport in Porous Media and Fractured Rock*. VCH, Weinheim, 1995.

[85] P. N. Sen, C. Scala, and M. H. Cohen. A self-similar model for sedimentary rocks with application to the dielectric constant of fused glass beads. *Geophysics*, 46:781–795, 1981.

[86] M. C. Serreze, M. M. Holland, and J. Stroeve. Perspectives on the Arctic's shrinking sea-ice cover. *Science*, 315:1533–1536, 2007.

[87] R. A. Shuchman and R. G. Onstott. Remote sensing of the polar oceans. In W. O. Smith, editor, *Polar Oceanography, Part A, Physical Science*, pages 123–169. Academic Press, 1990.

[88] A. H. Sihvola and J. A. Kong. Effective permittivity of dielectric mixtures. *IEEE Trans. Geosci. Remote Sensing*, 26(4):420–429, 1988.

[89] D. Stauffer and A. Aharony. *Introduction to Percolation Theory, Second Edition.* Taylor and Francis Ltd., London, 1992.

[90] A. Stogryn. An analysis of the tensor dielectric constant of sea ice at microwave frequencies. *IEEE Trans. Geosci. Remote Sensing*, GE-25(2):147–158, 1985.

[91] J. Stroeve, M. M. Holland, W. Meier, T. Scambos, and M. Serreze. 2007: Arctic sea ice decline: Faster than forecast. *Geophys. Res. Lett.*, 34:L09591, doi: 10.1029/2007GL029703, 2007.

[92] L. Tartar. Incompressible fluid flow in a porous medium. In E. Sanchez-Palencia, editor, *Non-Homogeneous Media and Vibration Theory, Volume 129 of Lecture Notes in Physics*, pages 368–377. Springer – Verlag, 1980.

[93] D. N. Thomas and G. S. Dieckmann. Antarctic sea ice − a habitat for extremophiles. *Science*, 295:641–644, 2002.

[94] D. N. Thomas and G. S. Dieckmann, editors. *Sea Ice: An Introduction to its Physics, Chemistry, Biology and Geology.* Blackwell, Oxford, 2003.

[95] S. Torquato. *Random Heterogeneous Materials: Microstructure and Macroscopic Properties.* Springer-Verlag, New York, 2002.

[96] S. Torquato and D. C. Pham. Optimal bounds on the trapping constant and permeability of porous media. *Phys. Rev. Lett.*, 92:255505:1–4, 2004.

[97] H. J. Trodahl, M. J. McGuiness, P. J. Langhorne, K. Collins, A. E. Pantoja, I. J. Smith, and T. G. Haskell. Heat transport in McMurdo Sound first-year fast ice. *J. Geophys. Res.*, 105(C5):11347–11358, 2000.

[98] M. R. Vant, R. O. Ramseier, and V. Makios. The complex-dielectric constant of sea ice at frequencies in the range 0.1–40 GHz. *J. Appl. Phys.*, 49(3):1264–1280, 1978.

[99] P. Wadhams. *Ice in the Ocean*. Gordon and Breach Science Publishers, Amsterdam, 2000.

[100] W. F. Weeks and S. F. Ackley. The growth, structure and properties of sea ice. In N. Untersteiner, editor, *The Geophysics of Sea Ice*, pages 9–164. Plenum Press, New York, 1986.

[101] W. F. Weeks and A. J. Gow. Crystal alignments in the fast ice of Arctic Alaska. *J. Geophys. Res.*, 85(C2):1137–1146, 1980.

[102] J. S. Wettlaufer, M. G. Worster, and H. E. Huppert. Natural convection during solidification of an alloy from above with application to the evolution of sea ice. *J. Fluid Mech.*, 344:291–316, 1997.

[103] O. Wiener. Die theorie des mischkorpers fur das feld des stationaren stromung. *Abhandl. Math., Phys. Klasse Königl. Sacsh. Gesel. Wissen*, 32:509–604, 1912.

[104] D. P. Winebrenner, J. Bredow, A. K. Fung, M. R. Drinkwater, S. Nghiem, A. J. Gow, D. K. Perovich, T. C. Grenfell, H. C. Han, J. A. Kong, J. K. Lee, S. Mudaliar, R. G. Onstott, L. Tsang, and R. D. West. Microwave sea ice signature modeling. In F. D. Carsey, editor, *Microwave Remote Sensing of Sea Ice, Geophysical Monograph 68*, pages 137–175. American Geophysical Union, 1992.

[105] P. Wong, J. Koplick, and J. P. Tomanic. Conductivity and permeability of rocks. *Phys. Rev. B*, 30:6606–6614, 1984.

[106] A. P. Worby, P. W. Griffin, V. I. Lytle, and R. A. Massom. On the use of electromagnetic induction sounding to determine winter and spring sea ice thickness in the Antarctic. *Cold Reg. Sci. Tech.*, 29:49–58, 1999.

[107] D. Zhang and E. Cherkaev. Padé approximations for identification of air bubble volume from temperature or frequency dependent permittivity of a two-component mixture. *Inverse Problems in Science and Engineering*. In print.

[108] D. Zhang and E. Cherkaev. Reconstruction of the spectral function from effective permittivity of a composite material using rational function approximations. Submitted.

[109] J. Zhu, A. Jabini, K. M. Golden, H. Eicken, and M. Morris. A network model for fluid transport in sea ice. *Ann. Glaciol.*, 44:129–133, 2006.